



HAL
open science

Microstructures, Water Contents, and Seismic Properties of the Mantle Lithosphere Beneath the Northern Limit of the Hangay Dome, Mongolia

Sylvie Demouchy, Andrea Tommasi, Dmitri Ionov, Katherine Higgie, R. W. Carlson

► **To cite this version:**

Sylvie Demouchy, Andrea Tommasi, Dmitri Ionov, Katherine Higgie, R. W. Carlson. Microstructures, Water Contents, and Seismic Properties of the Mantle Lithosphere Beneath the Northern Limit of the Hangay Dome, Mongolia. *Geochemistry, Geophysics, Geosystems*, 2019, 20 (1), pp.183-207. 10.1029/2018GC007931 . hal-02069249

HAL Id: hal-02069249

<https://hal.science/hal-02069249>

Submitted on 15 Mar 2019

HAL is a multi-disciplinary open access archive for the deposit and dissemination of scientific research documents, whether they are published or not. The documents may come from teaching and research institutions in France or abroad, or from public or private research centers.

L'archive ouverte pluridisciplinaire **HAL**, est destinée au dépôt et à la diffusion de documents scientifiques de niveau recherche, publiés ou non, émanant des établissements d'enseignement et de recherche français ou étrangers, des laboratoires publics ou privés.



RESEARCH ARTICLE

10.1029/2018GC007931

Key Points:

- Tariat mantle rocks are chemically and texturally homogeneous, well annealed, and hydrogen poor
- There is no evidence for recent major viscoplastic deformation, abnormal thermal gradient, or partial melting in the lithospheric mantle
- The samples have moderate seismic anisotropy with fast *S* wave polarization marking flow directions in the mantle

Supporting Information:

- Supporting Information S1

Correspondence to:

S. Demouchy,
sylvie.demouchy@umontpellier.fr

Citation:

Demouchy, S., Tommasi, A., Ionov, D., Higgle, K., & Carlson, R. W. (2019). Microstructures, water contents, and seismic properties of the mantle lithosphere beneath the northern limit of the Hangay Dome, Mongolia. *Geochemistry, Geophysics, Geosystems*, 20, 183–207. <https://doi.org/10.1029/2018GC007931>

Received 28 AUG 2018

Accepted 21 NOV 2018

Accepted article online 13 DEC 2018

Published online 8 JAN 2019

©2018. The Authors.

This is an open access article under the terms of the Creative Commons Attribution-NonCommercial-NoDerivs License, which permits use and distribution in any medium, provided the original work is properly cited, the use is non-commercial and no modifications or adaptations are made.

Microstructures, Water Contents, and Seismic Properties of the Mantle Lithosphere Beneath the Northern Limit of the Hangay Dome, Mongolia

S. Demouchy¹ , A. Tommasi¹ , D. Ionov¹, K. Higgle¹, and R. W. Carlson²

¹Géosciences Montpellier, CNRS and Université Montpellier, Montpellier, France, ²Department of Terrestrial Magnetism, Carnegie Institution for Science, Washington, DC, USA

Abstract To constrain the deformation, thermal evolution, and seismic properties of the mantle lithosphere beneath the Hangay Dome, we have analyzed the microstructures, crystal preferred orientations (CPO), and hydrogen concentrations of olivine and pyroxenes of 50 mantle xenoliths carried up by Cenozoic basalts from Zala, Haer, and Shavaryn-Tsaram from Tariat, Mongolia. Most xenoliths are medium- to coarse-grained spinel-lherzolites, but four contain garnet + spinel. Coarse granular, highly annealed microstructures predominate. The microstructures are associated with well-developed CPO, typical of deformation under high temperature, moderate pressure, and dry conditions. The hydrogen concentrations in olivine, orthopyroxene, and clinopyroxene are low and range around 5, 75, and 147 ppm H₂O wt, respectively. Together, microstructures and CPO indicate that ductile deformation was followed by static recrystallization, which has annealed the microstructures but preserved the CPO and, hence, the anisotropy of physical properties. Lack of correlation between annealing and equilibrium temperatures suggest that the annealing is due to a long quiescence episode since the last deformation episode. Here, there is not evidence that the formation of Hangay Dome is associated with recent deformation in the lithospheric mantle. Calculated seismic properties show moderate seismic anisotropy, with fast propagation of *P* waves and polarization of *S* waves parallel to the flow direction and low birefringence for *S* waves propagating obliquely to the flow plane. The results are consistent with weak *P* wave anomalies but not with the strong low *S* wave velocity anomalies predicted by some tomographic models or with the high conductivity inferred from magnetotelluric data for the lithospheric mantle beneath the Hangay Dome.

1. Introduction

The Hangay region in central Mongolia is characterized by a massif oriented NW-SE, 800- by 500-km wide, with a plateau-like topography culminating at ~4,000 m, commonly called the *Hangay Dome*. Its elevated topography, combined with late Cenozoic volcanism, and slightly elevated heat flow led Windley and Allen (1993) to interpret the Hangay Dome as the surface expression of a mantle plume. Subsequently, the Hangay Dome was the focus of several tectonic, petrochemical, and geophysical studies. However, these studies do not reach consensus on the present-day mantle dynamics beneath the Hangay Dome. The age and the mechanisms involved in formation of this relief are still debated. We summarize below the major and most recent results and interpretations.

The Hangay Dome is kinematically distinct from its surroundings, which are currently deforming as a far-field response to the India-Asia convergence (Cunningham, 1998). Present-day tectonics in central Mongolia is dominated by strike-slip and transpressional deformation in the Altai belt and in large-scale faults north and east of the Hangay Dome, such as the Bolnai fault, and by rifting in the Baikal region (Cunningham, 2001). However, no Cenozoic thrust faults or transpressional deformation, which could accommodate the uplift, are observed in the flanks of the dome. Cenozoic deformation in the Hangay Dome is limited to a few extensional faults with a dominant NE-SW trend in its southern border and crest, which show no evidence of connection to deep-seated detachments (Cunningham, 2001). These field observations are consistent with recent thermochronologic results (i.e., U-Th/He on bedrock apatite), which indicate that the Hangay Dome exhumation is Mesozoic (early Cretaceous, ~122 ± 24 Ma; McDannell et al., 2018).

The northern border of the Hangay Dome hosts a late Cenozoic volcanic field composed of low-volume eruptive centers, some of which carry mantle xenoliths to the surface. The composition of the lavas indicates that

they result from low partial melting degrees (Barry & Kent, 1998) and neither their He isotopic compositions (Barry et al., 2007) nor the long duration of scattered low-volume eruptions (Ancuta et al., 2018) are suggestive of a mantle plume source. Petrochemical studies on the xenoliths (Ionov, 2007; Ionov et al., 1998a; Ionov & Hofmann, 2007) have reported homogenous fertile compositions in the mantle lithosphere and equilibrium temperatures and pressures consistent with an ~80-km-thick lithosphere. The mantle xenolith's equilibrium temperatures are coherent with the slightly abnormal heat flow of 60–80 mW/m² measured in the Hangay Dome (Khutorskoy & Yarmoluk, 1989; Lysak & Dorofeeva, 2003), which also suggest a geotherm slightly hotter than the *normal* geotherm for a stable continental plate domain (i.e., 110-km-thick lithosphere). Two possibilities were proposed to explain the estimated geotherm: heating of the base of the lithosphere by hotter than average asthenospheric mantle or lithospheric delamination. A combination of the two scenarios is also plausible. The specifics of the Tariat volcanic field and of its xenoliths are further described in section 2.

In 2001–2003, the Mongolian-Baikal experiment, which transected the Hangay Dome in a N-S direction, passing near the volcanic field, produced the first regional characterization of the lithospheric structure and mantle deformation pattern in this region (Barruol et al., 2008; Calais et al., 2003; Petit et al., 2002, 2008; Tiberi et al., 2008; Vergnolle et al., 2007). Joint inversion of gravity and teleseismic data has imaged a domain with low seismic velocities and densities between 60- and 125-km depth beneath the Hangay Dome, with a possible westward dipping continuation up to 225 km (Tiberi et al., 2008). SKS data revealed a homogeneous NW-SE trending structural fabric, which was interpreted as encompassing both the lithospheric mantle and the asthenosphere due to the predominance of delay times >1.5 s (Barruol et al., 2008). The observed fast SKS polarization is parallel to the trend of the late Paleozoic belts, which formed the lithosphere in this region by accretion of microcontinents and island arcs around the Siberian craton (Zorin, 1999), and to the trend of the major active faults south and north of the dome (Cunningham, 2001). The SKS-deduced mantle flow direction is, however, at 20°–30° of the absolute plate motion in central Mongolia in the HS3-Nuvel-1A hotspot reference frame, suggesting local deflection of the asthenospheric flow by the Siberian craton root (Barruol et al., 2008). This study concluded that the Siberian craton played a major role in establishing the seismic anisotropy pattern in Mongolia, via its influence on both the past and present mantle deformation in the region (Barruol et al., 2008). However, variability in delay times over short range suggests heterogeneity of the shallow deformation, in particular beneath the Hangay Dome.

Recent adjoint (full-waveform) tomography models and receiver function analyses at the scale of East Asia (Chen et al., 2015) reported a 10- to 20-km upwelling and slightly high temperatures (+50 to +130 °C) in the mantle transition zone, as well as two low-velocity zones in the upper mantle beneath the dome: (1) a shallow (>120 km) broad V-shaped zone with low Vs (<–3%) and high Vp/Vs ratios and (2) a weak Vs anomaly (1%–2%) with a conduit-like shape linking the first anomaly to the one in the transition zone. This study also reported positive radial anisotropy (≤5%) in the shallow low-velocity anomaly and negative radial anisotropy along its edges.

The recent Hangay Dome seismic deployment in 2013–2014 (<http://www.ees.lehigh.edu/groups/mongolia>) provided additional geophysical constraints on the structure of the lithosphere and convecting mantle beneath the dome. Receiver function analysis points to a 43- to 57-km-thick crust and to gradual thinning of the lithosphere from the Gobi Altai to the northern part of the dome (Cui et al., 2017). The lithosphere thickness beneath the Hangay Dome ranges from 72 to 75 km, being shallowest in the north (Tariat region). In contrast to Chen et al. (2015), receiver function analysis using this regional data set indicates a thickness for the mantle transition zone similar to the global average, arguing against the hypothesis of a deep mantle plume centered beneath the Hangay Dome (Cui et al., 2017).

In addition to seismic investigations, magnetotelluric (MT) data were acquired along a 610-km long, NNE to SSW profile cross cutting the Hangay Dome, imaging a large low-resistivity zone (bulk resistivity 30–60 Ωm) beneath the dome at depths of 70–140 km (Comeau et al., 2018). Based on calculations by Gardés et al. (2014), for a temperature of 1200 °C, unrealistic water contents over 350 ppm H₂O by weight (ppm H₂O wt.) in olivine would be necessary to explain such low electrical resistivity. Therefore, Comeau et al. (2018) interpret the MT data as indicative of partial melting (~6% melt) at 70- to 120-km depth, possibly resulting from an asthenospheric upwelling, which would control the volcanism and support the regional uplift.

In summary, despite the large number of studies, the relations between the Hangay intracontinental uplift and the underlying mantle dynamics remain, to date, poorly understood. Geophysical models based on the various data sets are not fully consistent, in particular in their predictions for the shallow (50- to 120-km depth) mantle composition and structure. In this study, we determine the mineral modes, analyze the microstructures, and measure the crystal preferred orientations (CPOs) of peridotitic minerals in xenoliths from the Tariat region to further constrain the deformation, thermal evolution, and seismic properties of the lithospheric mantle beneath Hangay. We also quantify the hydrogen concentrations in olivine and pyroxenes for the first time for this region. High water contents may for instance allow for partial melting at shallow depths as inferred from the MT data (Comeau et al., 2018) even in the absence of major thermal anomalies.

2. Materials and Methods

2.1. Sampling and Previous Studies on Tariat Xenoliths

All mantle samples were collected in the late Cenozoic (Quaternary) Tariat volcanic district (48°09'N, 99°54'E), which outcrops in a 20 × 30-km area on the NE slope of the Hangay Dome (Figure 1). The Tariat volcanic district is composed of several eruption centers (cinder and lava cones and volcanic breccia outcrops) and lava flows (Figure 1b) and is exceptional for the abundance of mantle and crustal xenoliths (Ionov, 2007; Ionov & Hofmann, 2007).

In this study, we analyze peridotite xenoliths from three sites, which are, from north to south, the Zala volcano, the Haer volcano, and the Shavaryn-Tsaram volcanic breccia (location is abbreviated as Z, H, and Sh in sample names, respectively). The volcanic products erupted between 8 and <1 Ma (Ionov, 2007; Ionov et al., 1998b). The host rock for the peridotite xenoliths is an alkali basalt composed of olivine phenocrysts in a groundmass of plagioclase, olivine, clinopyroxene (cpx), oxides, and silicate glasses (Barry et al., 2003).

The petrogeochemistry of peridotite xenoliths from the Tariat region was previously studied by Press et al. (1986), Ionov (1986, 2007), Ionov et al. (1998b), and Ionov and Hofmann (2007). We provide here a brief summary of the main results of these studies. The Tariat mantle peridotites were reported to have uniform modal and major element compositions, both laterally (over a range of 10 to 20 km) and vertically (depth range of 45 down to 60 km). They are dominantly fertile spinel lherzolites, composed of olivine, orthopyroxene (opx), clinopyroxene (cpx), Al-Cr-spinel (sp), and very rare (1%) phlogopite, amphibole, apatite, alkali feldspar, and interstitial silicate glass. Phlogopite, amphibole, and apatite are often referred to as *hydrous* phases, but we prefer to call them *volatile bearing* as often they have low water contents and significant amounts of other volatiles (F, Cl, and CO₂ in apatites) as shown for Tariat xenoliths (Ionov et al., 1986, 1997). The type of volatile-bearing minerals was reported to be specific to each volcanic center, i.e., phlogopite at Shute locality and amphibole at Tsagan. Mantle xenoliths at Shavaryn-Tsaram and Zala also include very rare garnet + spinel lherzolites as well as spinel lherzolites with veins of garnet pyroxenites (Ionov et al., 1994).

Tariat peridotite xenoliths constitute one of the most fertile continental lithospheric mantle suites in the world (Ionov, 2002). The chemical compositions of the most fertile Tariat lherzolites are very close to the primitive mantle estimates reported by Palme and O'Neill (2003) with a whole rock $\text{Mg}/(\text{Mg} + \text{Fe}) \times 100 = 89.7$ overlapping the estimate for the primitive mantle. Modal composition and major element composition variations in the Tariat peridotite suite indicate low degrees of melt extraction from a primitive mantle at moderate depth (1–3 GPa, 33–100 km, Ionov & Hofmann, 2007). In addition, some Tariat peridotites were enriched in Fe by percolation of evolved silicate melts but with no or very little metasomatic effects on other major and minor elements or modal compositions.

The thermal state of the lithosphere beneath the Tariat field may be constrained from thermobarometric studies on the xenoliths. Pressure (P) and temperature (T) equilibrium conditions of lower crustal xenoliths suggest crustal thicknesses of 45–50 km (Ionov et al., 1998b; Stosch et al., 1995). Based on the P - T equilibrium conditions of the lower crustal and upper mantle garnet-bearing granulites, pyroxenites, and lherzolites, Ionov et al. (1998a) and Ionov (2002) defined the Cenozoic Tariat geotherm, which is consistent with a reduced heat flow of 38–40 mW/m² and a surface heat flow of 70–80 mW/m² as shown in Figure 2. This geotherm is in agreement with the present-day geotherm determined by Fullea et al. (2012) based on integrated geophysical-petrological inversions. This geotherm implies a lithosphere-



Figure 1. Schematic maps of (a) central and north East Asia showing the Siberian craton, North China Craton, and major sites of peridotite xenoliths in Cenozoic alkali basaltic volcanic fields and (b) of the Tariat volcanic field (shaded in gray) with the location of the volcanic cones and the sampling sites of the studied peridotite xenoliths (redrawn from Ionov, 2007; Ionov et al., 1998b). Note that the English transcriptions of the geographic names are chosen to render, as closely as possible, those used by the local Mongolian population (Ionov et al., 1998b).

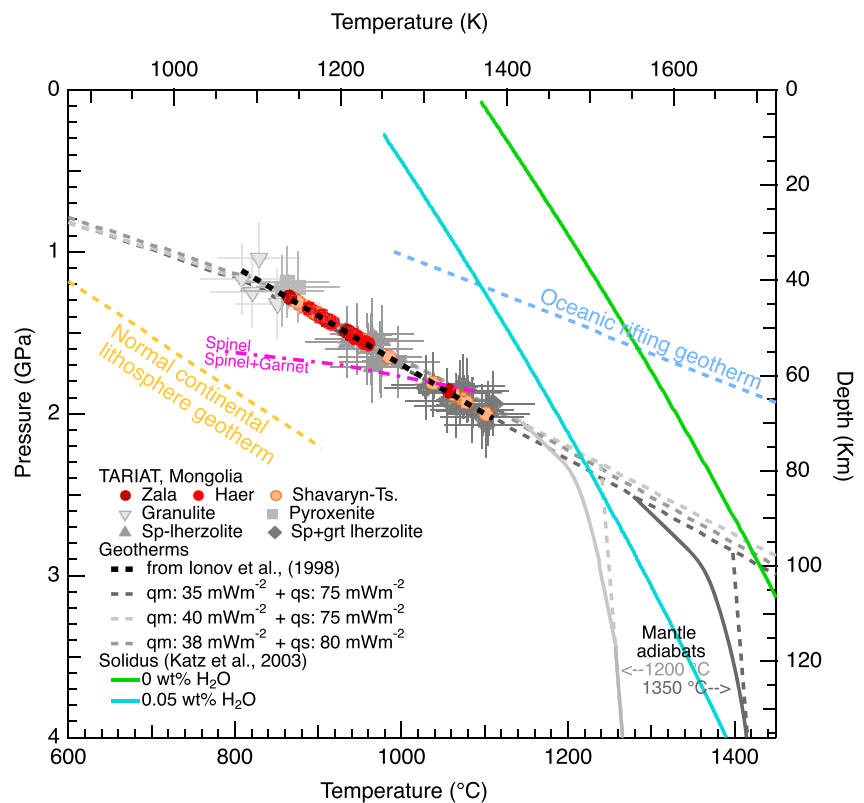


Figure 2. Pressure versus temperature diagram displaying the estimated equilibrium pressure and temperature for Tariat peridotites reported in previous petrogeochemical studies (Ionov et al., 1998b; Ionov, 2007) and for the peridotites studied here. The granulite data are originally from Stosch et al. (1995). The spinel to garnet + spinel transformation for fertile lherzolites was calculated for $Mg\# = 0.90$ and X_{Cr} in spinel = 0.075 (O'Neill, 1981, Ionov et al., 1998a). The dry and wet solidi for peridotite are from Katz et al. (2003; see their Figure 3). Note that 0.05 wt% H₂O = 500 ppm H₂O wt. Normal continental geotherm is for a 110-km-thick lithosphere (see main text for details).

asthenosphere boundary (LAB) at ~80-km depth, which is slightly deeper than the 72-km deep LAB below Tariat defined based on receiver function analysis (Cui et al., 2017).

Equilibrium temperatures for the spinel-peridotites studied here were obtained using the Ca-in-orthopyroxene thermometer (Brey & Köhler, 1990). Assuming a $P = 1.5$ GPa, the temperature estimates range from 875 to 1101 °C (Table 1). There are no reliable geobarometers for spinel-peridotites. If projected onto the Tariat geotherm from Ionov et al. (1998b) as shown in Figure 2, the equilibrium temperatures of the spinel peridotites correspond to pressures ranging from 1.28 to 2 GPa, thus to depths between 48 and 70 km. To characterize the microstructures and CPOs for the deeper sections of the lithosphere, we also analyzed garnet + spinel peridotites from Ionov et al. (1998b), whose equilibrium P conditions were determined based on the geobarometer of Nickel and Green (1985). According to Brey and Köhler (1990), temperature estimates have uncertainties of ± 50 °C for garnet-bearing peridotites, but up to ± 100 °C for garnet-free spinel peridotites (because of unknown P). As a consequence, the pressure estimations for the spinel peridotites have uncertainties of 0.5–0.8 GPa, that is, higher than the 0.22 GPa reported from geobarometry of garnet-bearing xenoliths (Ionov et al., 1998b). To further constrain the Tariat geotherm, the spinel to garnet transformation in fertile lherzolites (calculated for $Mg\# = 0.90$ and X_{Cr} in spinel = 0.075; following O'Neill, 1981, Ionov et al., 1998a) is also reported in Figure 2.

2.2. Microstructures and CPOs

We studied 46 xenoliths of spinel peridotites from a new extensive sampling of the Tariat district (Carlson & Ionov, 2013) and 4 garnet + spinel peridotites from a collection previously analyzed by Ionov et al. (1998b). Among the studied peridotites, 10 are from Haer, 10 from Zala, and 30 from Shavaryn-Tsaram (Figure 1 and

Table 1
Mineral Mode, Total Number of Grains (Nb Grains) From EBSD Maps, Petrological Indexes, Equilibrium Temperature, and Calculated Pressure

| Sample | Olivine | Opx | Cpx | Spinel | Nb grains | Volatiles-bearing minerals | Al ₂ O ₃ wt.% WR ^a | FeO wt.% WR ^a | Mg# ol ^a | T (°C) Ca-in-opx ^b | P (GPa) ^c |
|------------------------------------|---------|-----|-----|-----------|-----------|----------------------------|---|--------------------------|---------------------|-------------------------------|----------------------|
| Zala sp-peridotites | | | | | | | | | | | |
| Z11-1 | 53 | 25 | 19 | 3 | 466 | parg+phl | 2.95 | 7.98 | 0.893 | 939 | 1.51 |
| Z11-2 | 63 | 22 | 14 | 1 | 749 | no | 4.47 | 7.77 | 0.902 | 865 | 1.28 |
| Z11-5 | 65 | 21 | 14 | 1 | 552 | parg | 3.50 | 7.98 | 0.896 | 943 | 1.52 |
| Z11-9 | 65 | 21 | 13 | 1 | 545 | phl | 3.42 | 7.93 | 0.898 | 933 | 1.49 |
| Z11-12 | 61 | 27 | 11 | 1 | 430 | parg | 4.20 | 8.00 | 0.900 | 909 | 1.42 |
| Z11-15 | 53 | 29 | 16 | 2 | 690 | parg+phl | 4.15 | 8.37 | 0.894 | 934 | 1.49 |
| Z11-16 | 56 | 23 | 17 | 4 | 508 | phl | 4.44 | 8.24 | 0.891 | 913 | 1.43 |
| Z11-19 | 52 | 29 | 16 | 3 | 453 | parg+phl | 4.17 | 8.13 | 0.891 | 939 | 1.51 |
| Z11-20 | 56 | 23 | 19 | 2 | 667 | parg | 3.59 | 8.23 | 0.893 | 1057 | 1.86 |
| Z11-22 | 62 | 22 | 16 | <1 | 504 | phl | 3.86 | 8.15 | 0.897 | 946 | 1.53 |
| Haer sp-peridotites | | | | | | | | | | | |
| H11-1 | 55 | 31 | 12 | 2 | 416 | phl | 4.09 | 8.09 | 0.894 | 889 | 1.35 |
| H11-2 | 64 | 18 | 16 | 2 | 661 | parg+phl | 4.51 | 8.39 | 0.887 | 917 | 1.44 |
| H11-3 | 54 | 30 | 13 | 3 | 640 | parg+phl | 4.06 | 8.25 | 0.896 | 916 | 1.44 |
| H11-4 | 60 | 19 | 18 | 3 | 651 | parg+phl | 5.16 | 7.81 | 0.892 | 903 | 1.40 |
| H11-6 | 59 | 30 | 9 | 2 | 665 | parg+phl | 3.15 | 8.55 | 0.893 | 960 | 1.57 |
| H11-9 | 65 | 25 | 9 | 1 | 379 | phl | 4.25 | 8.24 | 0.891 | 905 | 1.40 |
| H11-12 | 62 | 19 | 17 | 2 | 531 | parg+phl | 2.06 | 9.28 | 0.896 | 955 | 1.56 |
| H11-17 | 80 | 9 | 10 | 1 | 323 | no | 4.19 | 8.36 | 0.891 | 946 | 1.53 |
| H11-22 | 61 | 19 | 17 | 3 | 539 | parg+phl | 0.62 | 7.65 | 0.920 | 945 | 1.53 |
| H11-25 | 86 | 10 | 3 | 1 | 211 | phl | 0.62 | 7.65 | 0.920 | 945 | 1.52 |
| Shavaryn-Tsaram sp-peridotites | | | | | | | | | | | |
| Sh11-3 | 61 | 23 | 14 | 2 | 1144 | parg+phl | 4.48 | 7.79 | 0.899 | 885 | 1.34 |
| Sh11-4 | 53 | 30 | 15 | 2 | 604 | parg | 3.37 | 8.20 | 0.899 | 948 | 1.53 |
| Sh11-5 | 67 | 19 | 12 | 2 | 779 | parg+phl | 2.09 | 7.69 | 0.901 | 872 | 1.30 |
| Sh11-7 | 67 | 21 | 11 | 1 | 491 | parg+phl | 6.69 | 7.57 | 0.913 | 1062 | 1.88 |
| Sh11-8 | 52 | 19 | 27 | 2 | 970 | parg+phl | 4.20 | 8.22 | 0.893 | 902 | 1.40 |
| Sh11-14 | 51 | 33 | 15 | 1 | 608 | parg+phl | 3.04 | 7.88 | 0.896 | 912 | 1.43 |
| Sh11-16 | 76 | 14 | 9 | 1 | 544 | n.d. | 4.65 | 7.92 | 0.907 | 890 | 1.36 |
| Sh11-17 | 61 | 20 | 17 | 2 | 714 | parg+phl | 3.36 | 8.39 | 0.899 | 937 | 1.50 |
| Sh11-20 | 66 | 20 | 12 | 2 | 544 | no | 2.24 | 7.69 | 0.898 | 903 | 1.40 |
| Sh11-22 | 74 | 20 | 5 | 1 | 390 | parg+phl | 3.22 | 8.64 | 0.912 | 909 | 1.42 |
| Sh11-27 | 72 | 19 | 8 | 1 | 395 | n.d. | 3.38 | 8.05 | 0.895 | 938 | 1.50 |
| Sh11-28 | 60 | 26 | 12 | 2 | 841 | parg+phl | 0.90 | 7.82 | 0.903 | 891 | 1.36 |
| Sh11-29 | 84 | 14 | 2 | <1 | 526 | parg+phl | 2.12 | 7.73 | 0.919 | 889 | 1.35 |
| Sh11-31 | 70 | 23 | 6 | 1 | 491 | no | 5.11 | 7.57 | 0.912 | 898 | 1.38 |
| Sh11-32 | 64 | 18 | 16 | 2 | 530 | parg+phl | 3.80 | 8.18 | 0.897 | 955 | 1.55 |
| Sh11-34 | 58 | 20 | 19 | 3 | 986 | n.d. | 4.39 | 8.23 | 0.899 | 865 | 1.28 |
| Sh11-37 | 51 | 35 | 13 | 1 | 620 | parg | 2.36 | 7.93 | 0.893 | 889 | 1.35 |
| Sh11-40 | 72 | 12 | 15 | <1 | 857 | parg+phl | 3.43 | 7.87 | 0.904 | 1073 | 1.91 |
| Sh11-49 | 76 | 14 | 9 | 1 | 526 | parg+phl | 2.88 | 7.93 | 0.908 | 897 | 1.38 |
| Sh11-51 | 69 | 20 | 10 | 1 | 507 | parg | 3.33 | 8.02 | 0.908 | 877 | 1.32 |
| Sh11-52 | 65 | 21 | 12 | 2 | 885 | parg+phl | 1.74 | 7.50 | 0.904 | 869 | 1.29 |
| Sh11-61 | 72 | 13 | 16 | 1 | 613 | parg+phl | 3.58 | 8.14 | 0.899 | 948 | 1.53 |
| Sh11-62 | 66 | 20 | 13 | 1 | 594 | no | 2.25 | 7.54 | 0.916 | 875 | 1.31 |
| Sh11-63 | 66 | 25 | 8 | 1 | 386 | parg+phl | 4.54 | 8.24 | 0.913 | 892 | 1.36 |
| Sh11-64 | 68 | 23 | 8 | 1 | 548 | parg | 3.74 | 8.07 | 0.893 | 985 | 1.65 |
| 11-4230-19 | 63 | 18 | 13 | 4 | 1337 | parg+phl | 3.92 | 8.53 | 0.897 | 900 | 1.39 |
| Shavaryn-Tsaram sp+grt peridotites | | | | | | | | | | | |
| 4334-11 | 63 | 20 | 14 | 0.2 + 2.1 | 347 | phl | 4.00 | 8.37 | 0.838 | 1062 | 1.88 |
| 4334-12(8) | 33 | 58 | 4 | 0.4 + 4.3 | 384 | no | n.a. | n.a. | 0.84 | 1038 | 1.81 |
| 4334-18 | 52 | 27 | 15 | 0.5 + 5.7 | 772 | phl | n.a. | n.a. | 0.889 | 1078 | 1.93 |
| 53389 | 49 | 14 | 28 | 0.6 + 7.5 | 975 | phl | 4.70 | 7.97 | 0.892 | 1101 | 2.00 |

Note. WR = whole rock; n.a. = not analysed; n.d. = not determine; the xenoliths samples were too small to perform whole rock analyses.

^aChemical compositions from Ionov et al. (1998a). ^bBrey and Köhler (1990). ^cCalculated following Tariat's geotherm (Ionov et al., 1998b); see main text and Figure 2 for spinel peridotites following the equation (pressure (GPa) = 0.00302^atemperature (°C) -1.3292); and for garnet peridotites following Nickel and Green (1985).

Table 1). All xenoliths are >3–4 cm in size and very fresh. The microstructures and rock textures were observed using classic optical microscopy and scanning electron microscopy.

CPOs were determined by indexation of electron-backscattered diffraction patterns (EBSD) on a JEOL JSM 5600 SEM at the EBSD facility of Geosciences Montpellier (University of Montpellier). Working distance was ~25 mm, acceleration voltage was ~17 kV, and the beam current was 10 nA. We analyzed crystal orientations of olivine, diopside, enstatite, and spinel, and when present, phlogopite, pargasite, and pyrope using the Aztec software from Oxford Instruments HKL.

For each sample, we obtained crystallographic orientation maps covering almost entirely the thin section (usually 20 × 35 mm) with a sampling step size of 40, 50, or 60 μm, depending on grain size. Indexation rates in the raw maps range from 80% to 90%. Postacquisition data treatment consisted of (i) removing wild spikes; (ii) filling the non-indexed pixels which have up to eight identical neighbors with the same orientation; (iii) repeating this operation using respectively seven, six, and five identical neighbors; (iv) identifying the grains, that is, continuous domains characterized by an internal misorientation <15°; and (v) within each olivine crystal, searching and correcting for rare systematic indexation errors due to the olivine hexagonal pseudo-symmetry, which results in similar diffraction patterns for orientations differing by a rotation of 60° around [100]. At each step, the operator verified the resulting orientation maps to avoid overextrapolation of the data. EBSD maps for all samples are presented in the supporting information (Figure S1).

CPO maps were treated with the MTEX toolbox in Matlab (Bachmann et al., 2010; Hielscher & Schaeben, 2008). The density of the orientation distribution function was calculated using an axisymmetric de la Vallée Poussin kernel with half-width of 10° (bandwidth of 28 in spherical harmonic coefficients). The strength of the CPO is characterized by the texture J index computed as the integral of the square of the orientation distribution function (Bunge, 1982). Here the J index is calculated using both one orientation data per pixel (J index Px) to not overestimate the potential contribution of small grains and the average orientation of the grains (one point per grain, J index oppg). For samples with variable grain sizes, the J index Px yields higher values than the J index oppg. We used the BA index, which was introduced by Mainprice et al. (2014), to characterize the symmetry of olivine CPO. This index allows classifying the olivine CPO into three types: (i) fiber-[010], characterized by a [010] point maximum and girdle distributions of [100] and [001] (BA index <0.35), (ii) orthorhombic, characterized by point maxima of [100], [010], and [001] (0.35 < BA index <0.65), and (iii) fiber-[100], characterized by a point maximum of [100] and girdle distributions of [010] and [001].

CPOs of olivine, orthopyroxene (opx), and clinopyroxene (cpx) are presented as pole figures. Densities of pole figures of the CPOs were normalized to a uniform distribution. Thin sections for EBSD analyses were not particularly cut parallel to a plane including the lineation and the normal to the foliation, since the latter were often not visible in the hand samples. To allow for easy comparison between the CPOs of different samples, the CPO orientation data for all minerals were rotated to have the maximum concentration of the olivine [100] axes in the east or west direction of the pole figure and the maximum concentration of [010] axes close to the north or south. The analysis of (i) the relative intensity of the orientation of [100], [010], and [001] of olivine, (ii) the relations between olivine and pyroxene CPOs, and (iii) the relations between olivine CPO and shape-preferred orientation (SPO), when the latter could be observed in thin sections, indicates that for most samples the CPOs are calculated relative to deformation reference frame, thus relative to the orientation of the flow direction (lineation, oriented E-W in the pole figures) and to the orientation of the flow plane (foliation, normal is N-S in the pole figures).

We used the grain detection method in MTEX (Bachmann et al., 2010) with a misorientation threshold of 15° to identify the grains based on EBSD data. Grains composed by less than 10 pixels were not considered in the microstructural analysis (grain sizes and shapes). The grain sizes are two-dimensional (2-D) values estimated as the diameter for a circle with equal area (i.e., arithmetic grain size is based on an equivalent diameter circle from the 2-D data and the area-weighted grain size is equal to $[\sum(\text{equivalent diameter} \times \text{grain area})]/\text{total area}$). Aspect ratios are minimum values, since they are 2-D estimates measured in sections with variable orientations relatively to the deformation reference frame. We choose to use area-weighted values for characterizing the grain size and aspect ratio of olivine and pyroxenes in the different samples, since (1) they give closer values to the visual estimate when observing the thin section than the arithmetic averages and (2) to maintain consistency with seismic properties, which depend on

volume fractions and not on the number of grains along the wave path. We characterize the sinuosity of the grain boundaries by the shape factor. It is defined as the perimeter of the grain divided by the perimeter of a circle with an identical area. The misorientation angle of each pixel relative to the mean orientation of the grain (M2M) and the grain orientation spread, which is the standard deviation of the misorientation within a grain, were calculated to quantify the intracrystalline orientation gradients, which are a proxy of the dislocation density. Both the intragranular misorientation and the sinuosity of grain boundaries should decrease in response to recrystallization.

2.3. Seismic Properties

Seismic properties were calculated using the CPOs of olivine, opx, and cpx, and, when present, garnet and their respective modal content estimated from EBSD maps (Mainprice, 1990). The elastic constant tensors for all spinel peridotites were calculated at a pressure 1.5 GPa (~48 km of depth) and a temperature of 925 °C, corresponding to the average conditions representative of the shallow mantle lithosphere beneath Tariat (Figure 2). The seismic properties of the garnet + spinel peridotites were calculated at a pressure of 2 GPa and a temperature of 1070 °C, which are representative of the deep mantle lithosphere beneath Tariat. The elastic constants of olivine, orthopyroxene, clinopyroxene, and garnet single crystals and their pressure and temperature derivatives are from Abramson et al. (1997), Chai et al. (1997a, 1997b), and Sang and Bass (2014). A Voigt-Reuss-Hill averaging was applied in all calculations.

Average seismic properties for the lithospheric mantle beneath the northern Hangay Dome were calculated by averaging the elastic constant tensors of all spinel peridotite samples and of all garnet + spinel samples using the CPO data rotated into a common structural reference frame, thus considering a geographically coherent orientation of the foliation and lineation for all samples. These average properties therefore represent maximum estimates of the seismic anisotropy, which may be produced in the spinel and garnet stability fields of the lithospheric mantle beneath the Tariat field, if the studied xenoliths provide a representative sampling of the lithospheric mantle.

2.4. Fourier Transform Spectroscopy

The quantification of hydrogen concentration in selected crystals of olivine, opx, and cpx was performed by unpolarized Fourier transmission infrared (FTIR) spectroscopy in transmission mode. Prior to FTIR measurements, millimeter-sized grains of olivine, opx, and cpx were double-polished by hand using a polishing jig and diamond-lapping films with a micrometer grid size ranging from 30 to 0.5 μm . During polishing, the samples were held in place by thermoplastic adhesive (crystal bond). Afterward, several successive baths of pure acetone prior to FTIR analyses dissolved the adhesive and cleaned the samples. Final thickness ranged from ~500 μm up to 2.5 mm and are reported in Table S1.

The infrared (IR) spectra were acquired using a Bruker IFS 66v spectrometer, equipped with an MCT detector (Mercury Cadmium Telluride) cooled with liquid nitrogen, using a Global light source and a KBr/Ge beam splitter, coupled to a microscope (HYPERION 3000 Bruker microscope; see Denis et al., 2018, for details). Analyses were performed at ambient temperature and pressure, under a flux of H_2O - CO_2 -free purified air through the entire microscope. FTIR analyses were acquired in the mid-IR frequency range (between 5,000 and 700 cm^{-1}) by accumulating 256 scans at a resolution of 4 cm^{-1} and with a squared aperture, with 200 or 100 μm of wideness. Analyses were performed for 3 to 15 different random orientations of each grain (by manually rotating the grain), and the spectra were averaged for each grain to compensate for any significant anisotropy of the IR bands. Hydrogen concentrations per grain, mineral, and per xenolith are reported in Table S1.

To ease comparison of our results with previous studies, we used two calibrations: (1) we used a frequency-dependent calibration (Paterson, 1982), which quantifies the concentration of hydroxyl C_{OH} as a function of ζ (the orientation factor, which equals one third for unpolarized measurements), $k(\nu)$, which is the absorption coefficient for a given wavenumber ν , and X_i the density factor. The latter parameter is chemistry dependent; it equals 2,698 ppm wt H_2O for olivine, 2,812 ppm wt H_2O for opx, and 2,752 ppm wt H_2O for cpx (Demouchy & Bolfan-Casanova, 2016); (2) we also used mineral-specific calibrations: Withers et al. (2012) for olivine and Bell et al. (1995) for pyroxenes.

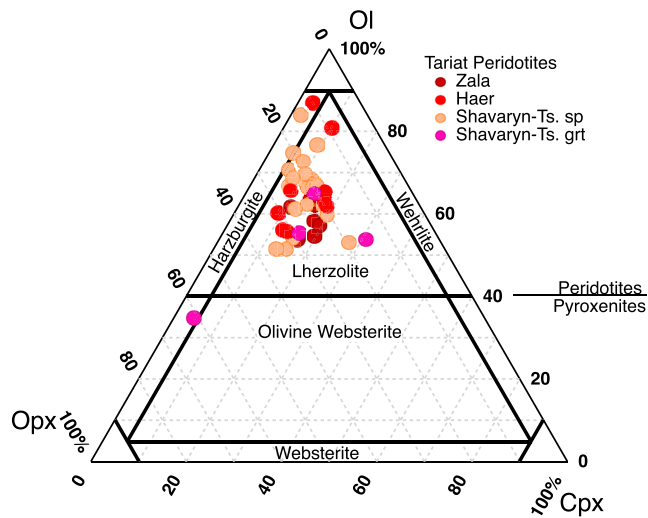


Figure 3. Ternary modal composition diagram for Tariat mantle xenoliths following the peridotite and pyroxenite classification of Streckeisen (1976).

After background correction, each FTIR spectrum was baseline corrected and normalized to 1 cm of thickness. The concentrations of hydrogen were calculated by integration of the IR spectrum between 3,650 and 3,100 cm^{-1} for olivine, 3,670–2,800 cm^{-1} for opx, and 3,770–3,000 cm^{-1} for cpx. The estimated error on the resulting water content is $\pm 15\%$; this error is due essentially to a combination of uncertainty in the empirical calibration laws and errors in sample thickness, the background spectrum, and the baseline subtraction. Note that the calibration from Paterson (1982) for unpolarized IR light on nonoriented crystals used here is likely to underestimate the absolute hydrogen concentration in olivine, whereas the calibration from Bell et al. (2003) using polarized IR light on oriented crystals overestimates it (Withers et al., 2012). Following F erot and Bolfan-Casanova (2012), a factor of 3 can be used to convert the hydrogen concentrations in olivine obtained with the Paterson (1982) calibration to values equivalent to those obtained with the method of Bell et al. (2003), and a factor between 1.8 and 2 can be used to convert them to values equivalent to those obtained with the calibration by Withers et al. (2012). The homogeneity of hydrogen concentration within crystals has been tested by unpolarized FTIR analyses at rims and centers of grains or by performing transects across grains when possible.

3. Results

3.1. Modal Compositions

Previous studies have already reported that the modal compositions of mantle xenoliths from the different Tariat eruption centers (i.e., Zala, Shute, Haer, Tsagan, and Bosko) are similar (Ionov, 2007). Indeed, based on our EBSD maps, the xenolith population in this study is essentially composed of lherzolites (Figure 3), with only three harzburgites (H11-25, Sh11-22 and Sh11-29) and one pyroxenite (garnet + spinel olivine orthopyroxenite 4334-12(8)). The modal composition of 4334-12 differs from the one previously reported for this sample (garnet + spinel lherzolite, Ionov, 2007) since the sample is veined and the studied thin section partially encompasses the vein. The modal compositions obtained in this study are reported in Table 1. The EBSD maps have permitted to identify that among the 50 studied xenoliths, 42 contain small volume fractions (<1%) of volatile-bearing minerals, most commonly pargasitic amphibole (amph) and phlogopite (phl); sample 4230-19 contains ~1.5% of euhedral phlogopite, as reported in Table 1. Phlogopite and apatite were previously reported as components of metasomatic veins in Shavaryn-Tsaram xenoliths (Ionov et al., 1997). Some xenoliths contain rare interstitial silicate glass and silicate glass pockets as also previously reported from Shavaryn-Tsaram and Zala peridotites (Ionov et al., 1994).

3.2. Microstructures

All peridotite xenoliths are medium to coarse grained. They are characterized by polygonal olivine crystals, which are notably clear of internal deformation features except for widely spaced subgrains and rare undulose extinction (Figure 4). A single garnet + spinel peridotite (4334-18) has a different microstructure, characterized by olivine crystals with undulose extinction, closely spaced subgrains, and grain boundaries with short-wavelength serrations. The area-weighted average olivine grain sizes are 2.03, 2.55, and 2.03 mm for xenoliths from Zala, Haer, and Shavaryn-Tsaram, respectively (Figure 5a and Table 2). Very large, centimeter-size olivine crystals are observed in olivine-rich layers in several spinel peridotites (e.g., H11-25). Some garnet + spinel peridotites and spinel peridotites display tabular microstructures, marked by a SPO of olivine crystals flattened normal to the [010] axis (e.g., H11-2, H11-20, and 4334-11, Figure 4), but in most spinel peridotites olivine tends to be equiaxed or have low aspect ratios of 1.4 to 2.0 with no clear SPO (Figure 5a).

Orthopyroxenes are also coarse and have irregular shapes. The average area-weighted opx grain sizes are 2.32, 1.97, to 1.95 mm for Zala, Haer, and Shavaryn-Tsaram, respectively (Figure 5a and Table 2). Clinopyroxenes are usually finer grained than opx. The average area-weighted cpx grain sizes are 1.17, 1.09, to 1.03 mm for Zala, Haer, and Shavaryn-Tsaram, respectively. Note that the area-weighted

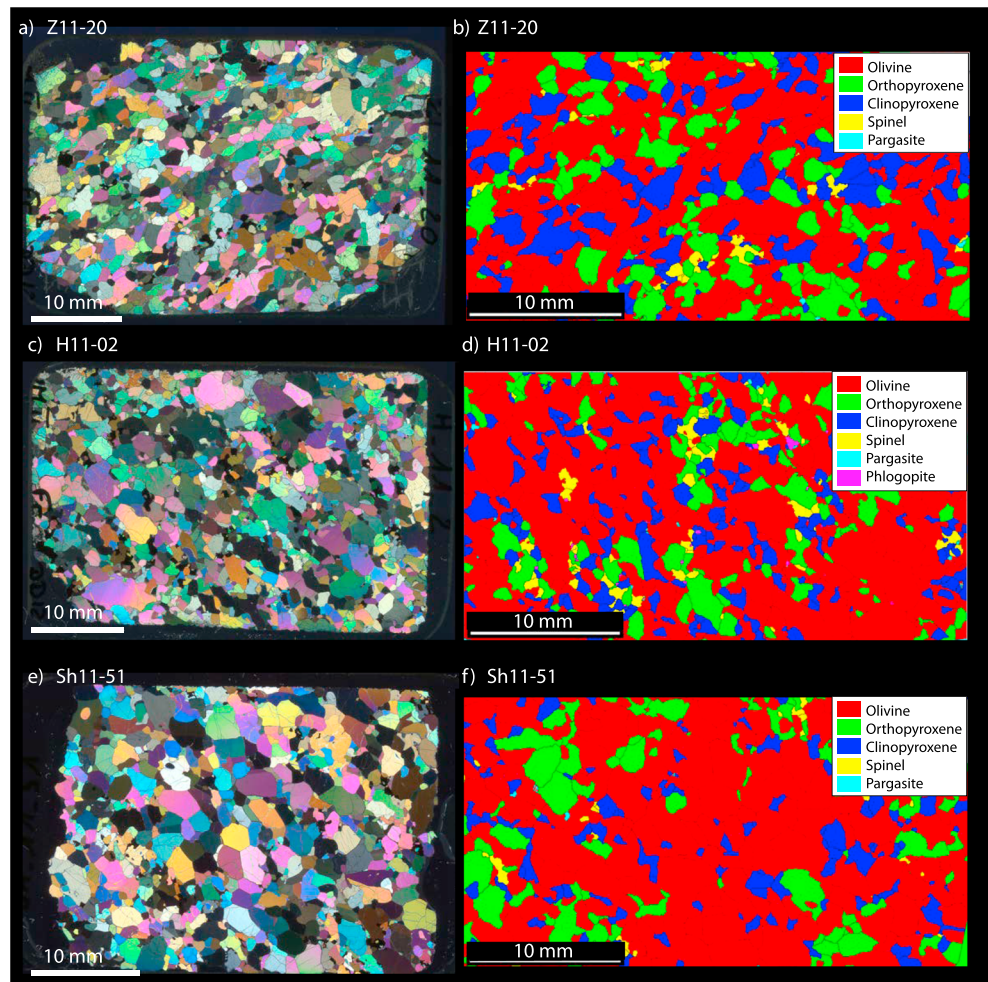


Figure 4. Microphotographs of representative thin sections in crossed-polarized light, and corresponding EBSD maps, illustrating typical microstructures of the Tariat peridotite xenolith suite: (a and b) samples Z11-20, (c and d) H11-02, and (e and f) Sh11-51.

average grain size is 2.1, 2.3, and 1.6 times higher than the arithmetic average grain size for olivine, opx and cpx, respectively. Clinopyroxenes also have irregular shapes. In general, pyroxene-olivine interface boundaries are more curved than pyroxene-pyroxene boundaries. The average area-weighted aspect ratios for both orthopyroxene and clinopyroxene in spinel peridotites yield very homogenous values between 1.60 and 1.71 (Figure 5a and Table 2).

Spinel has dominantly holly-leaf shapes. It occurs mainly in aggregates with orthopyroxene and clinopyroxene (Figure 4). In several samples spinel grains are aligned, marking the lineation (e.g., H11-22, Sh11-14, Sh11-52, and Z11-20; see Figure 4). Garnet only occurs in pyroxene-rich domains. It usually surrounds spinel crystals up to 0.5 mm wide. In sample 4334-18, garnet has no spinel cores but has small polygonal spinel crystals along the contacts with pyroxenes. Kelyphite rims, when present, are thin.

The EBSD maps permit the quantification of several microstructural features, reported in Table 2 and shown in Figure 5. We use the shape factor to discriminate samples with a well-equilibrated texture (i.e., straight grain boundaries) from samples with serrated or bulging grain boundaries. For olivine, the area-weighted average shape factors range from 1.59, 1.64, and 1.62 for Zala, Haer, and Shavaryn-Tsaram peridotites, respectively. Orthopyroxene shows slightly higher area-weighted average shape factors (1.70, 1.61, and 1.68 for Zala, Haer, and Shavaryn-Tsaram, respectively). Low area-weighted average shape factors ~ 1.5 characterize the small clinopyroxene crystals from all three localities (Table 2; n.b.,

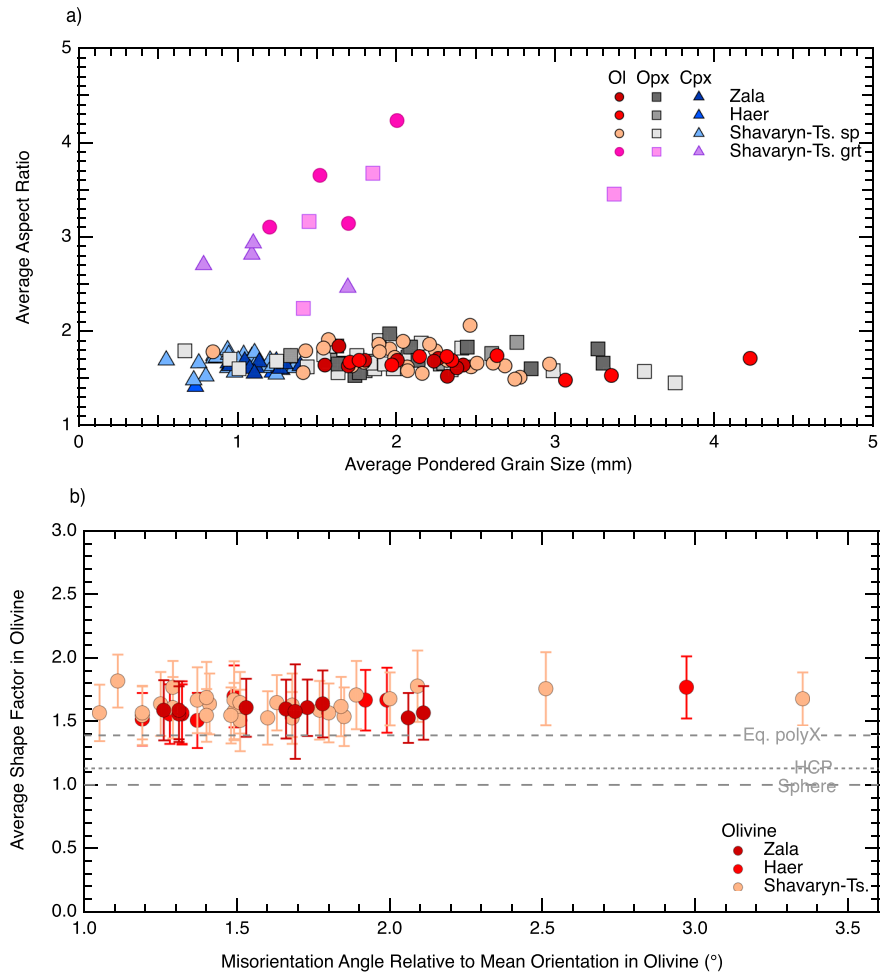


Figure 5. (a) Area-weighted average grain size as a function of the area-weighted average aspect ratio for olivine, orthopyroxene, and clinopyroxene in the Tariat peridotites. (b) Area-weighted shape factor as a function of M2M for olivine. Note that shape factor is the ratio of the perimeter of a grain over the perimeter of a circle with identical area; M2M is the average of the misorientation angle of each point within a grain relative to the mean orientation of the grain.

the area-weighted average shape factor is only 1.1 higher than the arithmetic mean shape factor, and the standard deviation is ~ 0.24 for all three minerals). The area-weighted shape factors for olivine in the Tariat peridotites are only slightly higher than those reported for a hot-pressed well-equilibrated polygonalnanoforsterite aggregate (e.g., Koizumi et al., 2010), which has a shape factor of ~ 1.39 (J. Gasc, personal communication, October 4, 2018). For reference, a perfect spherical grain has a shape factor of 1 and a perfect honeycomb hexagonal close-packed texture has a shape factor of 1.13.

The intragranular misorientation within the olivine grains was quantified using the crystallographic misorientation (angle) of each measurement point relative to the mean orientation of the grain (abbreviated as M2M). The olivine M2M values in Table 2 are average values over the whole EBSD map; all samples show low M2M values ($< 2.2^\circ$), consistent with the low density of intragranular deformation features observed optically, like subgrains or undulose extinction. The standard deviation of Mis2Mean, representing the dispersion in misorientation within all grains in a sample, is very high (it may reach up to 3° , being often higher than the mean value of M2M in the sample), indicating heterogeneous dislocation density distributions. Joint analysis of all quantitative microstructural parameters (Figure 5) highlights that except for the more elongated grain shapes in the garnet + spinel peridotites, there is no systematic variation in microstructure between peridotites from the three sampling sites.

Table 2

Apparent Weighted (Wt.) Average Grain Size, Aspect Ratio, and Shape Factor for Olivine, Opx and Cpx for the Three Localities, and the J Index per Pixel, BA Index per Pixel, the M Index, and the Average Misorientation to Mean Orientation (M2M)

| Sample | Weight average grain size | | | Weight average aspect ratio ^a | | | Weight average shape factor | | | Olivine | | | |
|---|---------------------------|-------|-------|--|------|------|-----------------------------|------|------|------------|-------------|---------|-------------|
| | Olivine | Opx | Cpx | Olivine | Opx | Cpx | Olivine | Opx | Cpx | J index px | BA index px | M index | Average M2M |
| Zala sp-peridotites | | | | | | | | | | | | | |
| Z11-1 | 1.549 | 1.738 | 0.953 | 1.64 | 1.53 | 1.63 | 1.53 | 1.55 | 1.45 | 4.61 | 0.64 | 0.080 | 2.06 |
| Z11-2 | 2.319 | 2.087 | 1.045 | 1.52 | 1.83 | 1.68 | 1.60 | 1.64 | 1.41 | 5.97 | 0.08 | 0.226 | 1.66 |
| Z11-5 | 2.262 | 1.957 | 1.118 | 1.71 | 1.97 | 1.61 | 1.61 | 1.62 | 1.46 | 4.05 | 0.48 | 0.123 | 1.73 |
| Z11-9 | 2.234 | 3.299 | 1.268 | 1.68 | 1.66 | 1.60 | 1.57 | 1.83 | 1.59 | 4.27 | 0.28 | 0.121 | 2.11 |
| Z11-12 | 1.800 | 2.846 | 1.136 | 1.69 | 1.60 | 1.67 | 1.58 | 1.94 | 1.52 | 4.02 | 0.50 | 0.062 | 1.69 |
| Z11-15 | 1.696 | 1.632 | 1.077 | 1.63 | 1.65 | 1.60 | 1.56 | 1.71 | 1.50 | 2.92 | 0.37 | 0.064 | 1.31 |
| Z11-16 | 2.004 | 3.266 | 1.335 | 1.69 | 1.81 | 1.71 | 1.59 | 1.78 | 1.59 | 3.10 | 0.46 | 0.046 | 1.26 |
| Z11-19 | 2.419 | 2.444 | 1.297 | 1.64 | 1.83 | 1.65 | 1.64 | 1.80 | 1.53 | 3.78 | 0.43 | 0.073 | 1.78 |
| Z11-20 | 1.637 | 1.766 | 1.395 | 1.84 | 1.56 | 1.63 | 1.59 | 1.57 | 1.53 | 3.35 | 0.48 | 0.132 | 1.31 |
| Z11-22 | 2.379 | 2.135 | 1.106 | 1.61 | 1.69 | 1.55 | 1.61 | 1.62 | 1.47 | 4.05 | 0.59 | 0.063 | 1.53 |
| Haer sp-peridotites | | | | | | | | | | | | | |
| H11-1 | 2.347 | 2.598 | 1.278 | 1.69 | 1.76 | 1.59 | 1.56 | 1.68 | 1.49 | 3.80 | 0.30 | 0.083 | 1.32 |
| H11-2 | 2.144 | 1.649 | 0.942 | 1.73 | 1.66 | 1.66 | 1.57 | 1.57 | 1.42 | 3.98 | 0.43 | 0.123 | 1.32 |
| H11-3 | 1.706 | 2.275 | 1.219 | 1.67 | 1.65 | 1.56 | 1.56 | 1.63 | 1.56 | 2.52 | 0.40 | 0.024 | 1.28 |
| H11-4 | 1.970 | 1.801 | 1.316 | 1.64 | 1.58 | 1.63 | 1.52 | 1.50 | 1.51 | 3.49 | 0.33 | 0.078 | 1.19 |
| H11-6 | 1.764 | 2.297 | 0.954 | 1.69 | 1.66 | 1.65 | 1.51 | 1.59 | 1.44 | 2.66 | 0.33 | 0.047 | 1.37 |
| H11-9 | 3.062 | 2.757 | 1.000 | 1.48 | 1.88 | 1.59 | 1.67 | 1.73 | 1.46 | 7.04 | 0.43 | 0.138 | 1.99 |
| H11-12 | 2.631 | 1.334 | 1.244 | 1.74 | 1.74 | 1.68 | 1.67 | 1.58 | 1.49 | 4.17 | 0.47 | 0.065 | 1.92 |
| H11-17 | 3.351 | 1.833 | 0.986 | 1.53 | 1.68 | 1.65 | 1.77 | 1.53 | 1.46 | 8.68 | 0.62 | 0.080 | 2.97 |
| H11-22 | 2.316 | 1.582 | 1.240 | 1.73 | 1.82 | 1.61 | 1.70 | 1.59 | 1.59 | 3.45 | 0.57 | 0.021 | 1.49 |
| H11-25 | 4.224 | 1.580 | 0.735 | 1.71 | 1.69 | 1.41 | 1.88 | 1.76 | 1.58 | 9.39 | 0.33 | 0.212 | 3.75 |
| Shavaryn-Tsaram sp-peridotites | | | | | | | | | | | | | |
| Sh11-3 | 1.428 | 1.245 | 0.756 | 1.79 | 1.68 | 1.66 | 1.57 | 1.54 | 1.49 | 6.23 | 0.11 | 0.255 | 1.05 |
| Sh11-4 | 1.957 | 2.103 | 1.049 | 1.81 | 1.76 | 1.65 | 1.61 | 1.75 | 1.51 | 3.43 | 0.29 | 0.053 | 1.29 |
| Sh11-5 | 1.888 | 2.022 | 0.851 | 1.86 | 1.60 | 1.74 | 1.64 | 1.77 | 1.57 | 5.58 | 0.16 | 0.201 | 1.25 |
| Sh11-7 | 2.469 | 2.985 | 1.025 | 1.62 | 1.58 | 1.62 | 1.58 | 1.64 | 1.46 | 4.70 | 0.59 | 0.096 | 1.49 |
| Sh11-8 | 1.571 | 1.751 | 1.162 | 1.91 | 1.72 | 1.61 | 1.64 | 1.73 | 1.53 | 2.74 | 0.57 | 0.041 | 1.41 |
| Sh11-14 | 1.892 | 3.559 | 1.205 | 1.78 | 1.57 | 1.69 | 1.53 | 1.82 | 1.50 | 3.53 | 0.49 | 0.099 | 1.60 |
| Sh11-16 | 2.245 | 1.980 | 1.048 | 1.79 | 1.60 | 1.65 | 1.54 | 1.47 | 1.52 | 7.00 | 0.32 | 0.199 | 1.85 |
| Sh11-17 | 2.041 | 1.542 | 1.220 | 1.89 | 1.75 | 1.63 | 1.67 | 1.75 | 1.53 | 3.32 | 0.50 | 0.036 | 1.49 |
| Sh11-20 | 2.207 | 2.410 | 1.038 | 1.86 | 1.82 | 1.75 | 1.62 | 1.80 | 1.49 | 4.88 | 0.42 | 0.119 | 1.84 |
| Sh11-22 | 2.776 | 1.891 | 0.800 | 1.51 | 1.90 | 1.52 | 1.65 | 1.72 | 1.38 | 6.00 | 0.19 | 0.230 | 1.51 |
| Sh11-27 | 2.505 | 2.343 | 1.090 | 1.66 | 1.59 | 1.73 | 1.59 | 1.75 | 1.50 | 3.68 | 0.61 | 0.028 | 1.77 |
| Sh11-28 | 1.793 | 1.699 | 0.850 | 1.67 | 1.64 | 1.71 | 1.67 | 1.64 | 1.58 | 5.38 | 0.14 | 0.208 | 1.37 |
| Sh11-29 | 2.743 | 0.951 | 0.724 | 1.49 | 1.70 | 1.48 | 1.71 | 1.45 | 1.36 | 4.33 | 0.70 | 0.136 | 1.89 |
| Sh11-31 | 2.319 | 2.072 | 0.937 | 1.69 | 1.72 | 1.80 | 1.69 | 1.74 | 1.53 | 5.27 | 0.38 | 0.131 | 1.40 |
| Sh11-32 | 2.681 | 1.750 | 1.124 | 1.63 | 1.74 | 1.68 | 1.63 | 1.58 | 1.48 | 3.79 | 0.43 | 0.042 | 1.68 |
| Sh11-34 | 1.412 | 1.437 | 1.004 | 1.56 | 1.62 | 1.69 | 1.57 | 1.53 | 1.50 | 5.66 | 0.10 | 0.256 | 1.80 |
| Sh11-37 | 2.067 | 3.752 | 1.296 | 1.62 | 1.45 | 1.61 | 1.55 | 1.72 | 1.48 | 3.84 | 0.26 | 0.059 | 1.19 |
| Sh11-40 | 1.540 | 1.009 | 1.356 | 1.82 | 1.60 | 1.61 | 1.51 | 1.42 | 1.44 | 4.11 | 0.35 | 0.175 | 1.51 |
| Sh11-49 | 2.607 | 1.861 | 0.939 | 1.66 | 1.60 | 1.61 | 1.65 | 1.70 | 1.51 | 6.85 | 0.44 | 0.200 | 1.63 |
| Sh11-51 | 2.069 | 1.925 | 0.981 | 1.58 | 1.65 | 1.56 | 1.53 | 1.58 | 1.42 | 5.81 | 0.20 | 0.195 | 1.68 |
| Sh11-52 | 1.718 | 1.834 | 0.868 | 1.63 | 1.66 | 1.72 | 1.55 | 1.80 | 1.51 | 4.90 | 0.18 | 0.223 | 1.40 |
| Sh11-61 | 2.462 | 1.623 | 1.107 | 2.06 | 1.84 | 1.77 | 1.78 | 1.66 | 1.59 | 3.31 | 0.62 | 0.029 | 2.09 |
| Sh11-62 | 2.161 | 2.155 | 0.944 | 1.55 | 1.87 | 1.75 | 1.55 | 1.68 | 1.48 | 6.40 | 0.30 | 0.214 | 1.48 |
| Sh11-63 | 2.962 | 2.079 | 1.041 | 1.65 | 1.74 | 1.65 | 1.76 | 1.62 | 1.50 | 8.79 | 0.25 | 0.219 | 2.51 |
| Sh11-64 | 1.988 | 1.632 | 1.244 | 1.72 | 1.56 | 1.54 | 1.57 | 1.46 | 1.54 | 3.36 | 0.69 | 0.039 | 1.19 |
| 4230-19 | 0.845 | 0.668 | 0.551 | 1.78 | 1.79 | 1.69 | 1.68 | 1.7 | 1.63 | 4.58 | 0.08 | 0.233 | 0.88 |
| Shavaryn-Tsaram sp grt peridotites | | | | | | | | | | | | | |
| 4334-11 | 2.002 | 1.850 | 1.089 | 4.23 | 3.67 | 2.81 | 1.82 | 1.84 | 1.76 | 7.98 | 0.33 | 0.257 | 2.00 |
| 4334-12 | 1.518 | 3.368 | 1.099 | 3.65 | 3.45 | 2.93 | 1.68 | 2.04 | 2.18 | 5.44 | 0.34 | 0.128 | 1.11 |
| 4334-18 | 1.201 | 1.413 | 0.786 | 3.10 | 2.24 | 2.70 | 1.77 | 1.98 | 1.69 | 2.50 | 0.45 | 0.013 | 3.35 |
| 53389 | 1.697 | 1.449 | 1.693 | 3.14 | 3.16 | 2.46 | 1.66 | 1.79 | 1.74 | 3.19 | 0.56 | 0.043 | 1.29 |

Note. The M index is defined as the difference between the observed distribution of uncorrelated misorientation angles and the distribution of uncorrelated misorientation angles for a random texture.

^aMinimum values, since not all thin sections were cut on the XZ plane (normal to the foliation and parallel to the lineation).

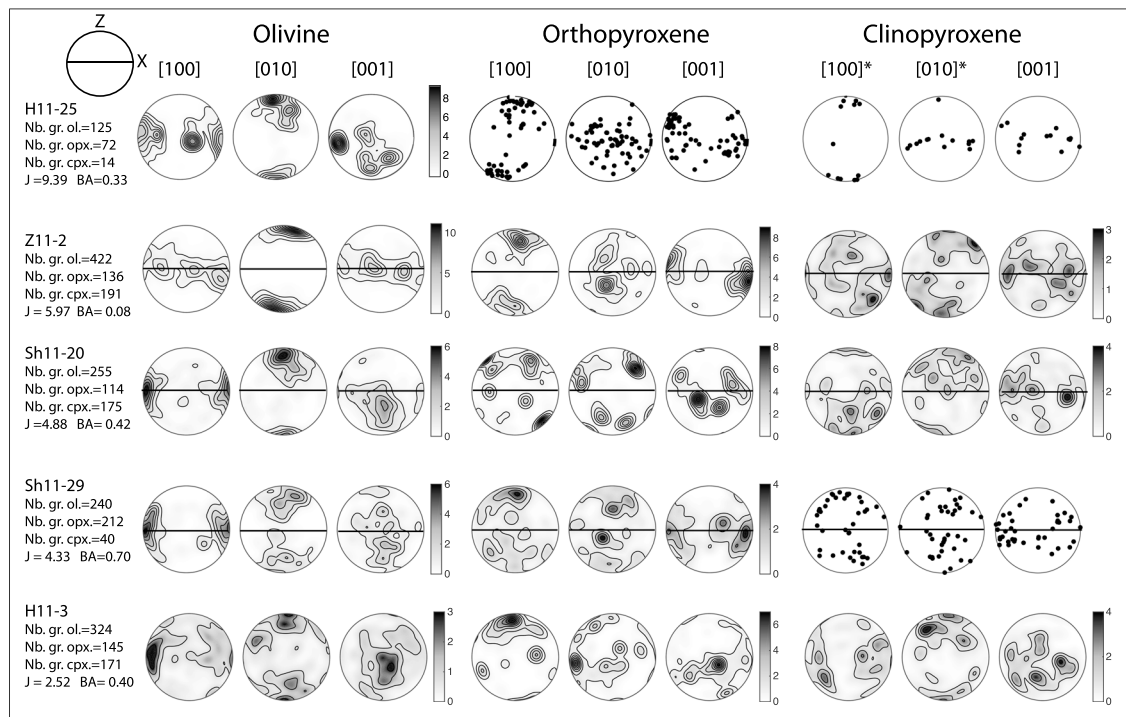


Figure 6. Olivine, orthopyroxene, and clinopyroxene crystal preferred orientations for a selection of representative samples (see main text for definitions of the J and BA indexes). Equal-area lower hemisphere stereographic projections; insert on the top left presents the reference frame. When less than 100 grains were analyzed for a given mineral phase, data are presented as points instead of density contours. When the orientation distribution of [100] of olivine is correlated with the orientation distribution of [001] of the pyroxenes, the three mineral phases are interpreted as syndeformed.

3.3. CPOs

All studied samples display well-developed olivine CPO, characterized by strong concentrations of both [100] and [010] axes of olivine as illustrated in Figure 6. We used the J and the BA indexes to characterize the strength and symmetry of the olivine CPO (Figure 7a). J index ranges from 2.5 to 9.4 (samples H11-3 and H11-25, respectively), indicating weak to rather strong olivine CPO. The BA index ranges from 0.1 to 0.7 (samples Z11-2 and Sh11-29, respectively), with equal proportions of fiber-[010] (BA indexes <0.35) and orthorhombic (BA indexes of 0.35-0.65) patterns. We have chosen to show in Figure 6 four CPO end-members and a sample representative of the average olivine CPO (Sh11-20, J index = 4.88, BA index = 0.42; n.b., the arithmetic average over the studied data set is J index = 4.71, BA index = 0.40).

Olivine [100] axes either form a clear maximum, which probably marks the lineation (orthorhombic patterns, characterized by BA indexes ranging from 0.35 to 0.65), or are dispersed in a girdle (fiber-[010] patterns, characterized by BA indexes <0.35). The [010] axes usually concentrate into a single maximum, which in the samples displaying a SPO marking a foliation is normal to it. All tabular samples are characterized by strong concentration of [010] normal to the flattening of the olivine crystals, but not all fiber-[010] CPOs are associated with a well-developed olivine SPO. In rare samples, [010] shows a weak dispersion in a plane normal to the [100] maximum (tendency toward a fiber-[100] pattern, BA index >0.65). The [001] axes are usually more dispersed than [100] or [010] (i.e., H11-25), but they either form a maximum normal to the [100] and [010] maxima or a girdle normal to the [010] maximum (fiber-[010] pattern, e.g., Z11-2 in Figure 6).

Pyroxene CPOs are usually more dispersed than the olivine CPO. Samples with the strongest pyroxene CPOs tend to display well-correlated olivine and pyroxene CPOs (cf. H11-25 and Sh11-29 in Figure 6), characterized by alignment of the concentrations of [001] axes of both pyroxenes with the maximum concentration of [100] axes of olivine, as well as alignment of the concentrations of [100] in orthopyroxene and of [100] or [010] axes in clinopyroxene with the maximum of [010] axes of olivine. This

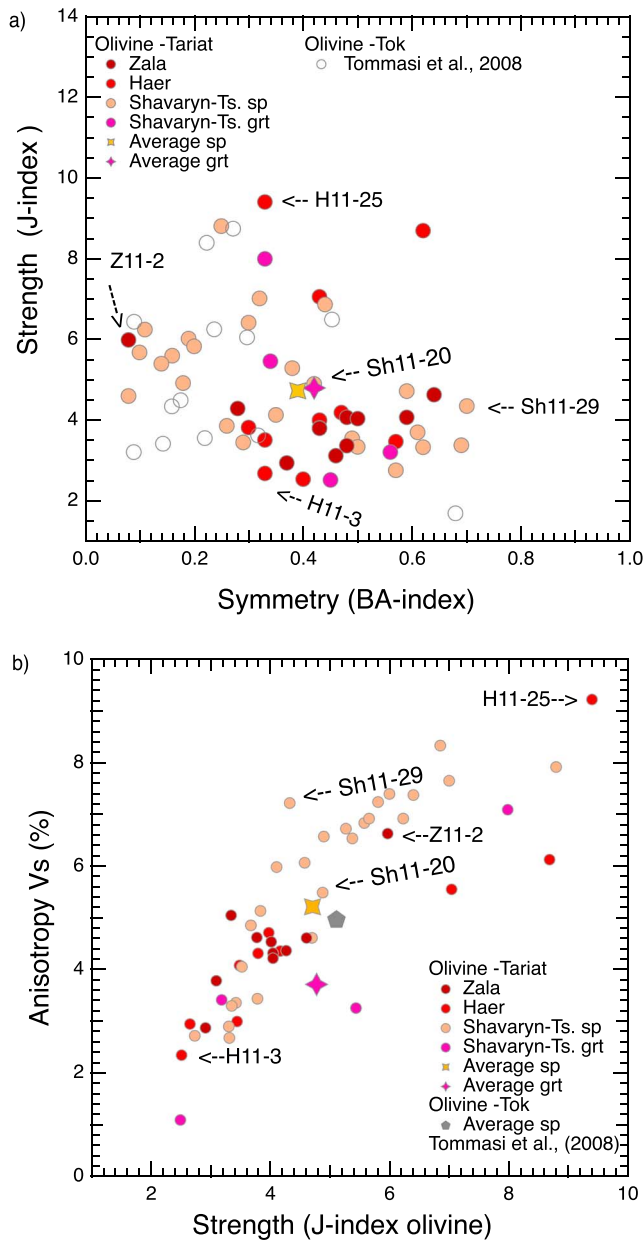


Figure 7. (a) Texture strength (J index) as a function of texture symmetry (BA index) of the olivine crystal preferred orientations of all studied Tariat peridotites. (b) Seismic anisotropy (V_2) as a function of texture strength (J index). See main text for details.

correlation suggests that all three phases were codeformed in the dislocation creep regime. A few samples show nevertheless pyroxene CPOs characterized by a concentration of [001] of one or both pyroxenes at high angle to the olivine [100] maximum (cf. H11-3 in Figure 6).

The analysis of (i) the relative intensity of the orientation of [100], [010], and [001] of olivine, (ii) the relations between olivine and pyroxene CPOs, and (iii) the relations between olivine CPO and SPO (when observed) indicates deformation by dislocation creep with dominant activation of the [100](010) slip system in olivine and [001](100) in orthopyroxene. Thus, both the maximum concentration of olivine [100] axes and of orthopyroxene [001] axes mark the flow direction and the maximum concentration of olivine [010] axes and of orthopyroxene [100] axes mark the normal to the flow plane even in the samples, which do not show a clear SPO. The seismic anisotropy data below are therefore presented relative to the deformation reference frame.

3.4. Seismic Properties

The seismic properties of samples H11-25 (strong orthorhombic olivine CPO), Sh11-29 (moderate strength fiber-[100] olivine CPO), Z11-2 (moderate strength fiber-[010] olivine CPO), and H11-3 (weak orthorhombic olivine CPO, see Figures 6 and 7) as well as the average seismic properties for all spinel peridotites and for the four garnet + spinel peridotites are shown in Figure 8 and reported in Table 3. The elastic constant tensors and densities used for calculating the seismic properties displayed in Figure 8 are provided in Table S2. Seismic anisotropy of the average garnet + spinel peridotites is lower than the average spinel peridotites since the former have weak to moderate olivine CPO (Figure 7b) and high pyroxene contents (Table 1). However, this might be a bias due to the low number (4) of garnet + spinel peridotites analyzed in this study.

Both the individual and the average samples show typical upper mantle seismic anisotropy patterns, with fast polarization of S waves and fast propagation of P waves parallel to the maximum concentration of olivine [100] axes, which, as discussed above, most probably marks the flow direction. The maximum P wave propagation anisotropy for the average spinel-peridotite and garnet + spinel peridotite is 6.4% and 3.6%, respectively. The maximum S wave polarization anisotropy for the average spinel-peridotite and average garnet + spinel peridotite is observed for waves propagating in the flow plane but at high angle to the flow direction, with values of 4.5% and 2.9%, respectively. Spinel peridotite H11-25, which has the strongest olivine CPO from the entire studied data set, displays maximum P wave propagation and S wave polarization anisotropies of 11.1% and 9.2% (Figure 7b and 8), respectively. Variations in olivine CPO sym-

metry (from fiber-010 to fiber-010 patterns) result in a change of the apparent null birefringence direction fiber S waves, which is at high angle to the foliation for samples with axial-[010] olivine CPO (Z11-2 in Figure 8) and at low angle to the lineation for samples with axial-[100] olivine CPO (Sh11-29 in Figure 8). Due to the high proportion of samples with fiber-[010] olivine CPO in the data set, both average samples show low birefringence for S waves propagating at high angle to the foliation.

Maximum V_{s1} and V_{s2} propagation anisotropies are 3.2% and 2.9% for the average spinel peridotite and 2% and 1.7% for the average garnet + spinel peridotite. If the flow direction is horizontal, V_{s1} is polarized horizontally and V_{s2} vertically, implying that Rayleigh waves are slower than Love waves. Moreover, Rayleigh wave velocities will display a 180° periodicity and the maximum possible anisotropies, whereas Love waves

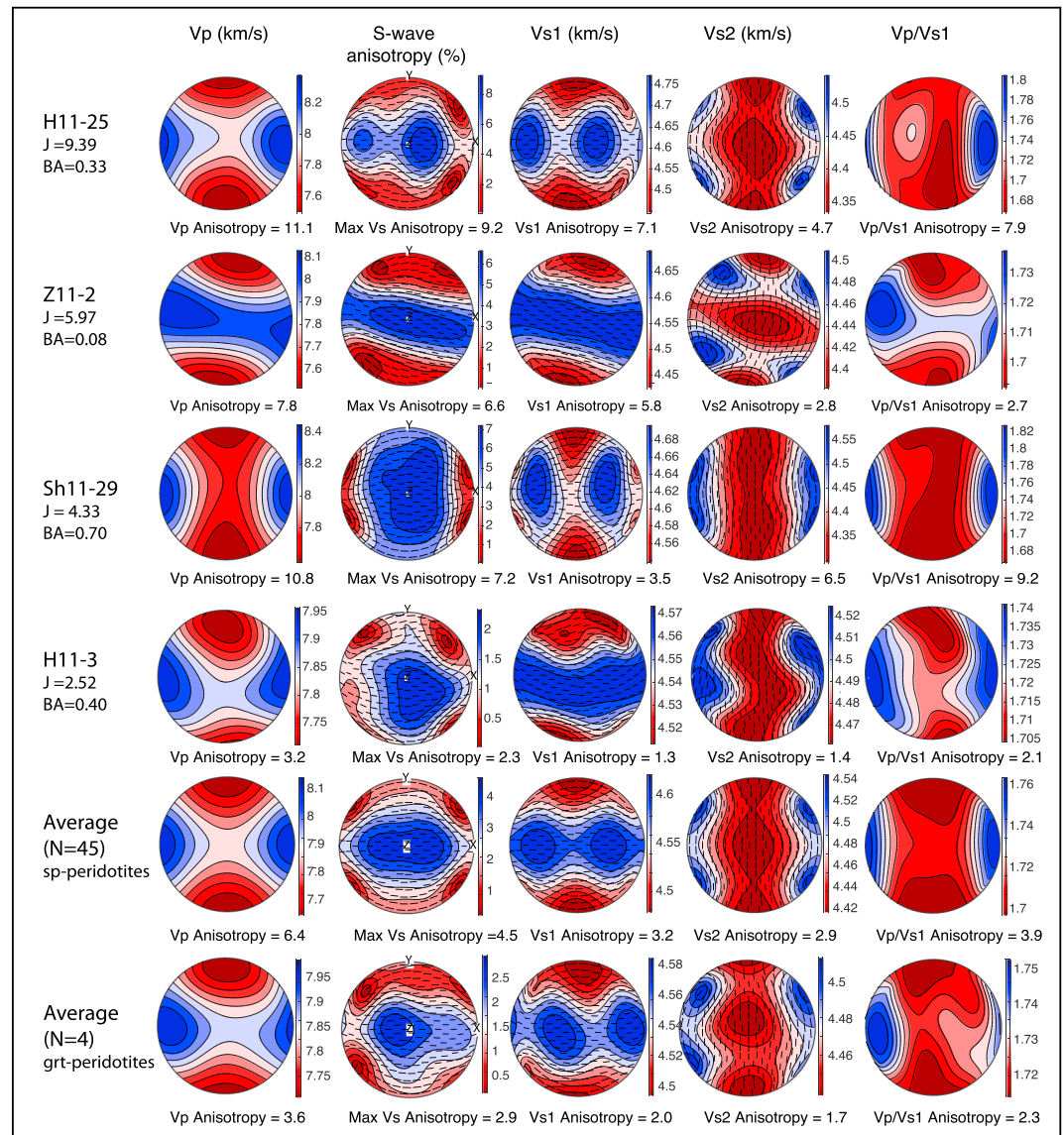


Figure 8. Average seismic anisotropy patterns calculated for selected peridotites (those with crystal preferred orientations presented in Figure 6) as well as for the average spinel peridotite and average garnet + spinel peridotite. Temperature and pressure used in the calculation are given in Table 3. From left to right: P wave velocity (V_p), S wave polarization anisotropy (AV_s) and the orientation of fast S wave polarization plane, S_1 wave velocities (V_{S1}), S_2 wave velocities (V_{S2}), and the V_p/V_{S1} ratio. Lower hemisphere stereographic projections; the reference frame is the same as in Figure 6.

will show a 90° periodicity and rather low anisotropy (average samples in Figure 8). Opposite patterns will be observed if the flow direction is vertical or steeply dipping.

Comparison between the mean P wave velocities for the average spinel peridotites and garnet + spinel peridotites (Table 3) highlights that they are almost constant within the mantle lithosphere: 7.87 km/s at ~ 45 km (925 $^\circ\text{C}$ and 1.5 GPa) to 7.84 km/s at ~ 60 km (1070 $^\circ\text{C}$ and 2 GPa), indicating that the change in modal composition (and thus density) and increase in pressure compensate for the influence of temperature increase on P wave velocity. Mean S wave velocities for the two depths are also similar (4.52 and 4.51 km/s; Figure 8 and Table 3), indicating that in the absence of attenuation, the effect of the temperature increase compensates those of the pressure increase and mineralogical change. V_p/V_s ratios for the average spinel- and garnet + spinel peridotites may show up to 3.9% and 2.3% of anisotropy (Figure 8). The highest V_p/V_s ratios

Table 3

Parameters Used to Calculate Seismic Properties and the Results of Three Samples (Strongest and Weakest Olivine CPOs, H11-25, H11-3, and Sh11-29) and the Average Properties for the 45 Spinel-Bearing Samples and for the 4 Garnet-Bearing Samples

| Sample | Temperature (°C) | Pressure (GPa) | Density | Vp mean (km/s) | AVp % | Vs mean (km/s) | AVs1% | AVs2% | Max Vp/Vs1 | Min Vp/Vs1 |
|-------------|------------------|----------------|---------|----------------|-------|----------------|-------|-------|------------|------------|
| H11-25 | 925 | 1.5 | 3.33 | 7.92 | 11.13 | 4.51 | 7.07 | 4.73 | 1.8 | 1.7 |
| Sh11-29 | 925 | 1.5 | 3.33 | 7.91 | 10.77 | 4.51 | 3.46 | 6.46 | 1.8 | 1.7 |
| Z11-2 | 925 | 1.5 | 3.31 | 7.87 | 7.84 | 4.52 | 5.82 | 2.84 | 1.7 | 1.7 |
| H11-3 | 925 | 1.5 | 3.31 | 7.84 | 3.17 | 4.52 | 1.32 | 1.40 | 1.7 | 1.7 |
| Average sp | 925 | 1.5 | 3.31 | 7.87 | 6.40 | 4.52 | 3.20 | 2.90 | 1.8 | 1.7 |
| Average grt | 1070 | 2 | 3.32 | 7.84 | 3.6 | 4.51 | 2.03 | 1.72 | 1.8 | 1.7 |

Note. CPO = crystal preferred orientation.

(≥ 1.75) are observed for waves propagating parallel to the flow direction and the lowest ratios (1.7), for waves propagating normal to the flow plane (Figure 8).

3.5. Hydrogen Concentrations

Over 142 grains from 11 spinel lherzolites (2 from Haer and 9 from Shavaryn-Tsaram) were analyzed by FTIR, providing estimates of hydrogen concentration in olivine (71 grains), orthopyroxene (56 grains), and clinopyroxene (12 grains). The grains were selected from separate fractions (> 0.5 mm) and handpicked to avoid weathered grains and select the larger ones, which allow for homogeneity to be checked. Therefore, all samples could not be analyzed.

The unpolarized absorption spectra of olivine from the Tariat xenoliths are shown in Figure 9a. There are two groups of absorption bands in olivine: group 1 from 3,598 to 3,420 cm^{-1} and group 2 from 3,420 to 3,280 cm^{-1} . The OH band at 3,572 cm^{-1} of group 1 has, in the vast majority of olivine grains, the highest absorbance. Bands from group 1 are always expressed, while bands from group 2 vary in their respective absorption intensities. This variation might result from a weak crystallographic orientation effect, which could not be completely overcome by averaging spectra obtained in different orientations of the same grain. However, the variation is more likely due to the low total absorption in this frequency range for several samples (i.e., Sh11-12, H11-17, Sh11-56, and Sh11-40 in Figure 9a). Measurements at rim and core positions or transects across clear olivine grains do not reveal heterogeneous hydrogen concentration (neither rim depletion nor rim enrichment). The IR spectra are typical of mantle-derived olivine (Demouchy et al., 2006, 2015; Denis et al., 2013, 2015, 2018; Miller et al., 1987; Peslier & Luhr, 2006). Water contents in olivine are homogeneous at the xenolith-scale but differ from xenolith to xenolith with values ranging from 1.2 to 9 ppm wt. H_2O (Table 4, calibration from Withers et al., 2012). These low water contents are typical of olivine from spinel peridotite xenoliths in alkali basalt (e.g., Demouchy & Bolfan-Casanova, 2016; Denis et al., 2013; Ingrin & Skogby, 2000; Peslier, 2010; Peslier et al., 2002; Peslier & Luhr, 2006; Soustelle et al., 2013; Wang, 2010).

The absorption spectra of both opx and cpx show at least three major absorption bands at 3,590, 3,521, 3,420, and 3,305 cm^{-1} and 3,627, 3,536 and 3,446 cm^{-1} , respectively (Figures 9b and 9c). Such absorption bands are typical of opx and cpx from peridotite xenoliths in alkali basalt (Bell & Rossman, 1992; Ingrin & Skogby, 2000; Peslier et al., 2002; Skogby, 2006; Xia et al., 2010; Yu et al., 2011). Hydrogen concentrations in opx and cpx display similar differences from xenolith to xenolith as in olivine, with average values of 75 (range 30–131) and 148 (range 87–277) ppm wt. H_2O for opx and cpx, respectively (Table 4). A ratio of 2 between opx and cpx water contents is observed, which is consistent with previous observations in xenoliths from many localities (Figure 10a, database from Demouchy & Bolfan-Casanova, 2016). The water content in pyroxenes in this study (< 300 ppm wt. H_2O in cpx) is low for mantle-derived pyroxenes (Figure 10a) but not that unusual for spinel peridotite xenoliths (e.g., Demouchy & Bolfan-Casanova, 2016; Satsukawa et al., 2017). The analysis of the distribution of hydrogen in opx as a function of hydrogen in olivine (Figure 10b) together with data from the review of Demouchy and Bolfan-Casanova (2016) leads to the same conclusion: opx in Tariat spinel-peridotites has low hydrogen concentrations. The hydrogen concentrations in Tariat pyroxenes are lower than values reported from other continental uplifts such as Colorado plateau (e.g., Peslier et al., 2002).

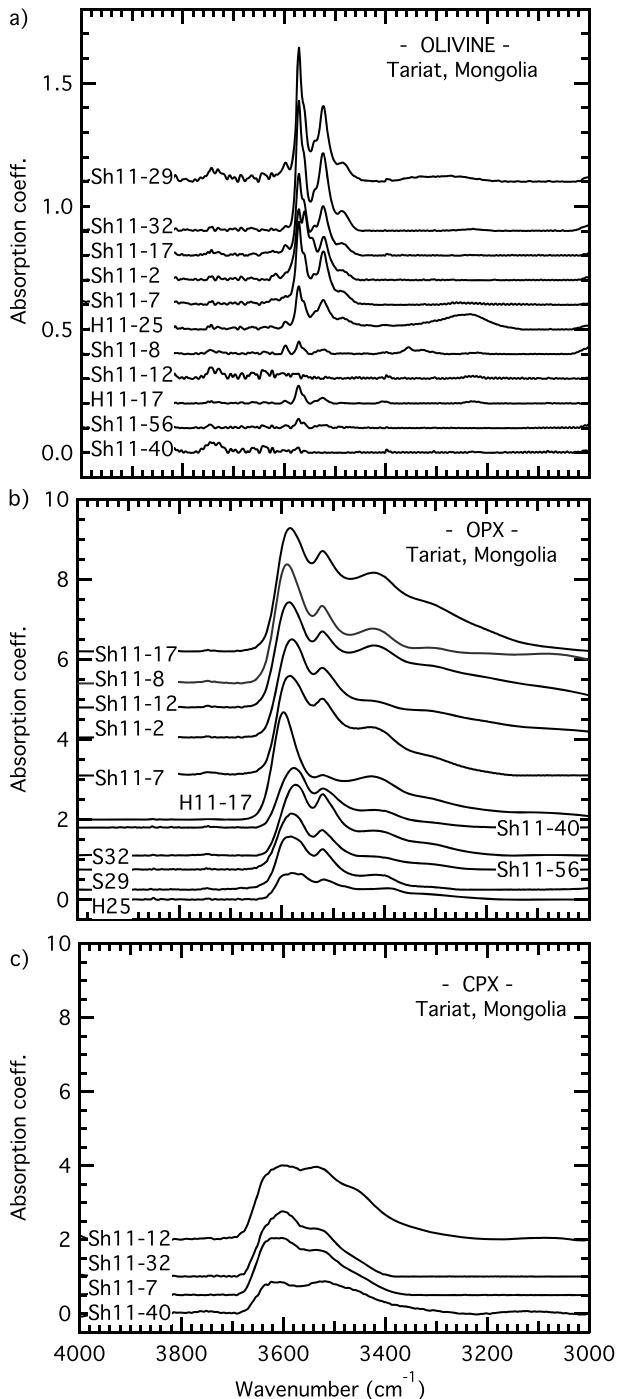


Figure 9. Unpolarized Fourier transmission infrared spectra of mantle-derived nominally anhydrous minerals from this study: (a) olivine, (b) orthopyroxene and (c) clinopyroxene. Spectra are normalized to 1 cm of thickness and offset for clarity.

Analysis of the hydrogen concentration in olivine as a function of Fo% (Figure 11a), which is a common petrological index, shows that the most Fe-rich compositions are the most depleted in hydrogen. Alumina content in opx is expected to influence the incorporation of hydrogen in opx and in coexisting olivine (e.g., Bali et al., 2008; Férot & Bolfan-Casanova, 2012; Gaetani et al., 2014; Mierdel et al., 2007). Here, hydrogen concentration in opx in the Tariat spinel-peridotites shows a rough positive correlation with alumina content (Figure 11b), which is in contradiction with the worldwide database (Demouchy & Bolfan-Casanova, 2016) but in agreement with experimental studies at high pressure and high temperatures (e.g., Férot & Bolfan-Casanova, 2012; Gaetani et al., 2014; Mierdel et al., 2007).

4. Discussion

4.1. Thermomechanical History

The microstructures of the Tariat mantle samples are uniform and well equilibrated. The polygonal grain shapes and the low density of intragranular deformation features, such as undulose extinction and subgrains, despite the clear CPOs, imply an important annealing (static recrystallization), which has erased the microstructures formed during the viscoplastic deformation responsible for the development of the CPO. High-stress microstructures recording a recent viscous deformation related to the surface uplift are not present among the studied xenoliths. Undulose extinction and closely spaced subgrains in olivine are observed in a single garnet + spinel peridotite (sample 4334-18). However, this sample has a coarse-granular microstructure, with no clear grain elongation, and shows no evidence for recrystallization, only serrated grain boundaries, implying that although it might have been subjected to high stress for a short time before extraction from the mantle, this sample did not undergo strong deformation. Absence of evidence for recent deformation in the lithospheric mantle beneath Tariat is consistent with geomorphological observations and thermochronologic results (i.e., U-Th/He on bedrock apatite), which indicate that the Hangay Dome exhumation is Mesozoic (early Cretaceous, $\sim 122 \pm 24$ Ma, McDannell et al., 2018).

The annealing at the origin of the well-equilibrated microstructures may result from (1) short exposure to elevated temperatures or (2) long annealing duration at moderate temperatures. The present-day geotherm beneath Tariat (Figure 2) is only slightly hotter than the one expected for a normal, 110-km-thick lithosphere. In addition, annealing has affected the entire studied xenolith suite and there is no correlation between annealing intensity and equilibrium temperature. Therefore, we propose that annealing in the Tariat lithospheric mantle does not result from a recent heating episode. The presence of interstitial melts, which could act as fast diffusion paths, may enhance annealing rates. Tariat mantle xenoliths have very fertile compositions, which in most cases are due to the absence or very low degrees of melt extraction from pristine mantle during the formation of the lithosphere

(e.g., Ionov & Hofmann, 2007), and for rare pyroxene-enriched samples could have resulted from melt-rock interactions leading to crystallization of pyroxenes. Yet, in most samples, pyroxene CPOs are coherent with the olivine CPO (Figures 8 and Figure S1), indicating that if any such *refertilization* occurred, most of it preceded the deformation.

Table 4
Hydrogen Concentrations in Olivine and Pyroxenes From Selected Mantle Xenoliths (Large Grain Size) From Tariat Region

| Sample | Olivine | | | Orthopyroxene | | | Clinopyroxene | | |
|---------|----------------------|------|---|----------------------|------|---|----------------------|------|---|
| | Average ^a | 1 SD | N | Average ^b | 1 SD | N | Average ^b | 1 SD | N |
| H11-17 | 1.2 | 0.4 | 7 | 82 | 11 | 3 | — | — | — |
| H11-25 | 5 | 2 | 5 | 23 | 5 | 3 | — | — | — |
| Sh11-2 | 9 | 3 | 7 | 73 | 16 | 6 | 99 | 20 | — |
| Sh11-7 | 6 | 1.8 | 7 | 93 | 31 | 7 | — | — | — |
| Sh11-8 | 1.4 | 0.4 | 6 | 112 | 27 | 6 | — | — | — |
| Sh11-12 | 1.7 | 0.5 | 5 | 131 | 17 | 4 | 277 | 75 | 4 |
| Sh11-17 | 6.5 | 1.5 | 8 | 111 | 25 | 7 | — | — | — |
| Sh11-29 | 8.5 | 3 | 8 | 30 | 10 | 6 | — | — | — |
| Sh11-32 | 8 | 2 | 4 | 64 | 15 | 6 | 128 | 18 | 4 |
| Sh11-40 | 1.2 | 0.5 | 7 | 44 | 16 | 5 | 87 | — | 1 |
| Sh11-56 | 1.7 | 1.7 | 7 | 66 | 29 | 6 | — | — | — |

Note. For normalized absorbance and hydrogen concentration based on the calibration of Paterson (1982); see Table S1 online. SD = standard deviation.

^aHydrogen concentrations based on the calibration of Withers et al. (2012). ^bHydrogen concentrations based on the calibration of Bell et al. (1995).

One may wonder if annealing at a temperature of 925 °C would be fast enough to explain the currently observed grain size (2–5 mm) in the Tariat mantle rocks if these rocks had experienced strong deformation during the Mesozoic, leading to grain refinement up to ~100 μm for olivine (i.e., to a recrystallized olivine grain size typical of mantle mylonites, e.g., Vauchez et al., 2012; Frets et al., 2014). Knowing that grain growth in silicate aggregates for this grain size range is dominantly controlled by lattice diffusion of Si (e.g., Dohmen et al., 2002; Dohmen & Milke, 2010; Hiraga et al., 2010), we may estimate the grain size evolution as a function of time. There is currently no experimental data available for the olivine grain growth rate in the temperature and composition range of the Tariat peridotites, but using a Si diffusion coefficient of $5.3 \times 10^{-28} \text{ m}^2/\text{s}$ at 925 °C from Dohmen et al. (2002), we obtain a characteristic (diffusion) distance of 2.9 μm for 120 Ma, thus well below the current grain size. Therefore, temperatures in the lithospheric mantle must have been higher to produce the observed annealed microstructures if strong deformation occurred in the lithospheric mantle in the Mesozoic. This implies that the geotherm might have been hotter and the lithosphere thinner in the past (e.g., during the Mesozoic) and that the deeper samples may correspond to a previous asthenospheric mantle, which was accreted to the lithosphere by cooling. This interpretation is consistent with the radiogenic isotopic composition of Tariat mantle samples, which are similar to modern mid-ocean ridge basalt (Carlson & Ionov, 2013) and thus suggest the accretion of a portion of fertile mid-ocean ridge basalt mantle beneath Tariat region. However, the fertile compositions of the majority of Tariat xenoliths argues against a very thin lithosphere or an abnormally hot mantle in the past, since the 1200 and 1350 °C mantle adiabats cross the dry peridotite solidus at ~40 and 90 km of depth, respectively (Figure 2).

The strong annealing hinders a thorough analysis of the deformation that predated it. Yet the preservation of (100) subgrain boundaries and of olivine CPO with strong [100] and [010] maxima point to deformation by dislocation creep with dominant activation of the high-temperature, low-pressure [100](010) slip system. The olivine and pyroxene CPO are correlated indicating a coherent deformation by dislocation creep of the three mineral phases with dominant activation of [100](010) in olivine, [001](100) in orthopyroxene, and [001](110) in clinopyroxene (e.g., Figure 6, sample H11-25). Activation of dominant [100] slip in olivine is also consistent with the low hydrogen concentrations measured in olivine (Figure 10b). Simple shear deformation accommodated by dominant [100] slip in olivine would mainly produce orthorhombic or fiber-[100] CPO patterns (Tommasi et al., 2000). The high proportion of fiber-[010] olivine CPO patterns within the Tariat peridotites might be a consequence of static recrystallization. Similar association of coarse-tabular microstructures and fiber-[010] olivine CPO patterns indeed has been reported in mantle xenoliths from the Tok volcanic field at the SE border of the Siberian craton (shown in Figure 7 for comparison). The Tok xenoliths also have evidence for well-developed annealing (Tommasi et al., 2008).

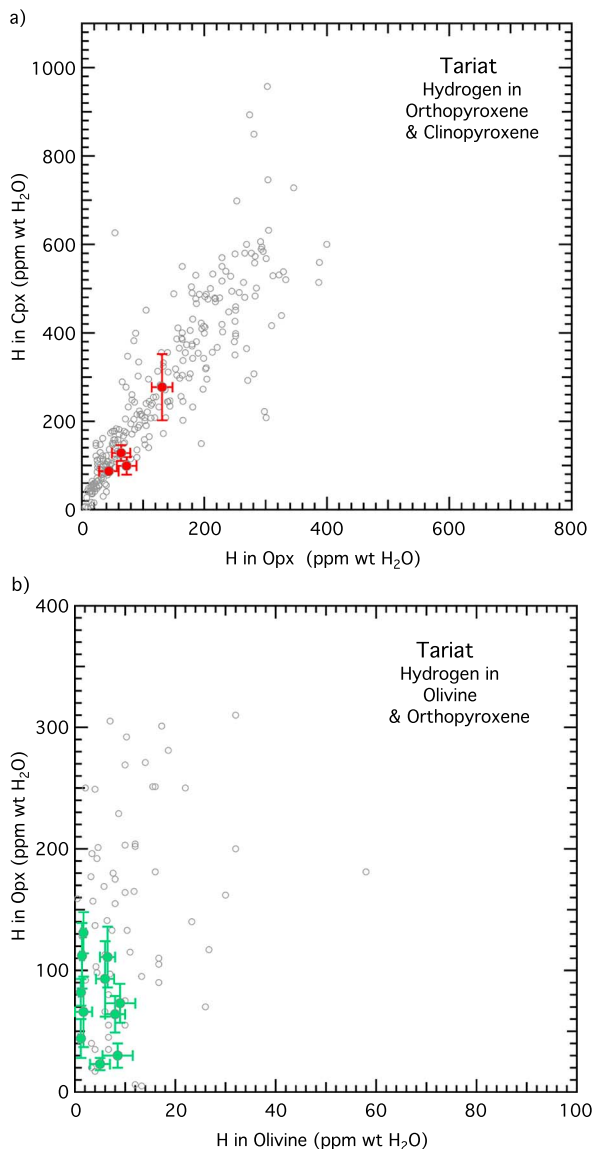


Figure 10. (a) Hydrogen concentrations in coexisting orthopyroxene and clinopyroxene (only four pairs) in mantle xenoliths from Tariat region; (b) hydrogen concentrations in coexisting orthopyroxene and olivine. Data based on other spinel peridotites from different localities worldwide from Demouchy and Bolfan-Casanova (2016) are also shown for comparison.

Transpression or deformation in the presence of partial melting may also produce fiber-[010] olivine CPO (Higgie & Tommasi, 2012, 2014; Qi et al., 2018; Tommasi et al., 1999). However, in the Tariat peridotites, fiber-[010] olivine CPO are not associated with girdle distributions of [001] axes of the pyroxenes (cf. sample Z11-2 in Figure 8), as they should if the CPO of both minerals were formed in response to transpression (Tommasi et al., 1999). Moreover, as discussed above, the well-correlated olivine and pyroxene CPOs of most Tariat peridotites suggest that if any reactive melt percolation occurred, it predated the deformation.

4.2. Partial Melting in the Lithospheric Mantle and Asthenosphere

The occurrence of Cenozoic volcanism points to partial melting in the asthenosphere. In the case of the Hangay area, the Cenozoic basaltic volcanism is composed of small volume eruptions of low-degree partial melts scattered in space and time (Ancuta et al., 2018) without any chemical features typically associated with intracontinental mantle plumes (e.g., Barry et al., 2007). There are only three possible causes for mantle melting: (1) increase of the temperature above the peridotite solidus, (2) decompression induced by asthenospheric upwelling, or (3) addition of volatile elements such as water (as hydrogen in the NAMS) or CO₂ (carbonate flux or carbon). The geotherm defined by the Tariat xenolith thermobarometry implies an 80- to 90-km-thick lithosphere and does not cross the dry solidus of a fertile peridotite (Figure 2). The solidus of a dry peridotite would be attained if the lithosphere below Tariat was as thin as inferred from receiver function analysis (72–75 km, Cui et al., 2017) for asthenospheric temperatures following a hot adiabat (1300 °C at the surface). However, such a shallow LAB is not consistent with the temperature and pressure conditions inferred from thermobarometry for the garnet + spinel lherzolites (in the spinel stability field), which equilibrated at depths of 60–70 km and temperatures ≤1100 °C (Figure 2, Table 1).

Volatiles may significantly reduce melting temperatures. At 2.5 GPa, the melting temperature of water-saturated lherzolite containing 200 ppm H₂O wt is 1100 °C (Green et al., 2014; Kovács et al., 2012). However, the studied peridotites contain very small amounts of hydrous minerals and the coexisting nominally anhydrous minerals do not hold a hydrogen concentration high enough to lower the solidus in a significant manner. The water content calculated for the Tariat peridotites using the measured mineral modes and the FTIR calibrations from both Bell et al. (1995) and Withers et al. (2012) is 38 ppm H₂O wt. based on nominally anhydrous minerals only, and 48 ppm H₂O wt. if 0.5% of amphibole containing 2 wt.% H₂O is included. If the presently studied xenoliths are representative, these data completely preclude partial melting in the lithospheric mantle (Figure 2). The results also imply that to induce melting, the asthenosphere beneath Tariat must have significantly higher volatile contents than the studied xenoliths.

The deep lithosphere and the asthenosphere beneath the Hangay Dome are characterized by high electrical conductivity, which was interpreted by Comeau et al. (2018) as most likely due to the presence of ~6% melt (see Yoshino et al., 2006, for experimental calibration). Nevertheless, to produce such high partial melting degrees at >70-km depth, abnormal mantle temperatures and/or compositions, not consistent with the present data, are required. Moreover, 6% melt would produce very strong low *S* velocity anomalies, which are not observed in most seismic tomography models (e.g., Lebedev et al., 2006; Tiberi et al., 2008). High melt contents in the sublithospheric mantle beneath the Hangay Dome are also not required by joint modeling

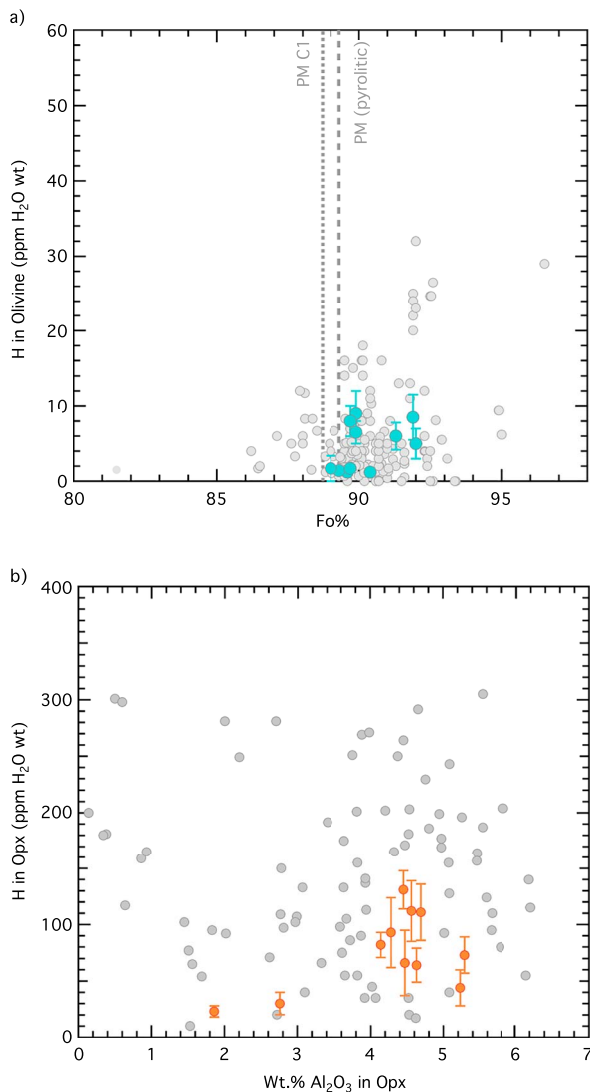


Figure 11. (a) Hydrogen concentrations in olivine as a function of the Fo% (i.e., $\text{Fo}\% = \text{Mg}/(\text{Mg} + \text{Fe}) \times 100$) in blue from this study. The value for primitive mantle (PM) (McDonough & Sun, 1955, Pyrolitic model 1 and CI) and (b) Hydrogen concentrations in orthopyroxene as a function of the Alumina content (Wt.%) in orange from this study. Data from other spinel peridotites from different localities worldwide from Demouchy and Bolfan-Casanova (2016) are shown as grey symbol for comparison.

(4.51 km/s; Table 3). This value is slightly higher (+0.8%) than V_s in the ak135-f model at 43- to 50-km depth (Kennett et al., 1995). However, we did not include the anelastic component in the calculation of the seismic properties of the xenoliths. This component is expected to decrease V_s , but it depends strongly on temperature, in particular above 1000 °C and on grain size (see Afonso et al., 2010; Faul & Jackson, 2005; Jackson & Faul, 2010). For the large grain sizes observed in our samples (2–2.5 mm) and for the estimated equilibrium temperatures (850–1100 °C), the expected decrease in the olivine shear modulus is very small (<1%; Jackson & Faul, 2010). The predicted S wave velocities and densities of our average samples are indeed very similar to the best fit of the integrated geophysical-petrological inversion surface wave-topography inversions for this region at lithospheric mantle depths by Fullea et al. (2012), which included anelastic effects.

Seismic velocity also varies with composition, yet, for reasonable mantle compositions, this effect is limited. For instance, a decrease in Fo% in olivine from 90 to 87 results in -1.25% S wave anomaly (Tommasi et al., 2004). The chemical composition of the Tariat mantle peridotites is very uniform with olivine Fo% ranging

of seismic velocities and topography (Fullea et al., 2012). The origin of the magneto-telluric anomalies reported by Comeau et al. (2018) remains thus unexplained.

4.3. Seismic Wave Velocities and Anisotropy

Most P wave tomography models point to lower than average seismic velocities in the shallow upper mantle beneath the Hangay Dome. Tiberi et al. (2008), Koulakov (2011), and Souza (2015) reported ΔV_p of -2% to -3% at depths of 80–100 km beneath the Hangay dome. Tariat is located at the northern limit of these low velocity anomalies, at the transition to a domain with normal velocities. The average spinel lherzolite mantle sample from Tariat has mean P wave velocities lower by 2.8% than the PREM model at 1.5 GPa (Dziewonski & Anderson, 1981) and lower by 2.0% than the ak135-f model at 43- to 50-km depth (Kennett et al., 1995). The data obtained here for the Tariat xenoliths thus explain well the observed low P wave anomalies with no need to invoke partial melting or abnormal heating of the lithosphere.

The densities (ρ) calculated for the average Tariat samples from mineral modes (3.31 g/cm³ for the average spinel peridotite and 3.32 kg/m³ for the average garnet + spinel peridotite; Table 3) are lower than those in the seismic reference models (at 40 km of depth, ρ : 3.379 g/cm³ for PREM, at 43 km of depth, ρ : 3.58 g/cm³ for ak135-f) and lower than typical values for uppermost peridotites (e.g., 3.349 g/cm³ for spinel peridotites and 3.31–3.399 for garnet peridotites, at standard temperature pressure conditions, see Lee, 2003). This is consistent with the low density anomaly detected in the joint gravity-seismic inversion beneath the northern part of the Hangay Dome at 80- to 125-km depth ($\Delta\rho = -0.02$ to 0.03 ; Tiberi et al., 2008).

For S waves, the interpretation is less clear. Seismic tomography studies based on surface waves (e.g., Lebedev et al., 2006; Lebedev & van der Hilst, 2008) propose that the Tariat region is located just on the western border of a major low-velocity V_s zone, identified at 60-km depth, which fades with increasing depth. Beneath the Tariat region specifically, V_s variations range from -4% to $+1\%$. This is consistent with body wave tomography predictions by Koulakov (2011) and by Souza (2015). In contrast, the recent joint tomography by Chen et al. (2015) predicts up to -6% V_s anomaly in the uppermost mantle (<100-km depth) beneath the Hangay Dome, and that this anomaly is well expressed beneath Tariat.

Mean S wave velocities predicted using the average Tariat spinel- and garnet + spinel peridotites at 45- and 61-km depth, respectively, are similar

between 89 and 92 and with a mean at 90 (Figure 11). Pyroxenites and refractory peridotites are rare among the Tariat xenoliths and cannot be significant components of the lithospheric mantle. Hydrogen embedded in point defects in olivine was also proposed to decrease seismic wave velocities, but very high concentrations, which may only be achieved in the lower part of the upper mantle, are necessary for a significant effect (Jacobsen, 2006). Olivines in the Tariat peridotites, have very low hydrogen contents, which have negligible effect on seismic velocities. The presence of melt also decreases seismic wave velocity; 1% of melt (interconnected or not) can generate a decrease of 1%–3% in V_p and 3–10% in V_s (see for a review Foulger et al., 2013). However, as discussed above, the equilibrium temperatures and pressures of the Tariat peridotites are well below the dry solidus (Figure 2) and the calculated whole rock water contents (0.0038 wt.% H_2O) are too low to trigger wet melting (see wet solidus for 0.05 wt.% H_2O in Figure 2). In summary, the Tariat xenolith compositions, microstructures, and CPOs are not consistent with the strongest low S wave velocity anomalies in the lithospheric mantle predicted by some body shear and surface wave tomographic results for the mantle beneath the Hangay Dome.

Concerning seismic anisotropy, Lebedev et al. (2006) and Chen et al. (2015) reported VS_H faster than VS_V with up to 5% of anisotropy in the lithospheric mantle beneath central Mongolia. This observation is consistent with the calculated average seismic properties of the Tariat peridotites if lineations, marking past flow directions in the lithospheric mantle, are subhorizontal (Figure 8). The calculated VS_1 for the average spinel peridotite and garnet + spinel peridotite, which corresponds in this case to VS_H , varies between 4.64 and 4.58 km/s depending on the backazimuth (Figure 8) and is in rather good agreement with the results from Lebedev et al. (2006) and Chen et al. (2015). In contrast, the calculated VS_2 , which corresponds in this case to VS_V , varies between 4.54 and 4.52 km/s (Figure 8), being significantly higher than the minimal values of $VS_V = 4.2$ km/s reported by Lebedev et al. (2006) and Chen et al. (2015) at 100-km depth, and still slightly higher than the $VS_V = 4.4$ km/s reported by Lebedev et al. (2006) at 50-km depth. The radial anisotropy of the average Tariat peridotites is therefore lower than that predicted for the sub-Tariat lithosphere from seismological data.

If the lineations are subhorizontal, steeply propagating body waves would sample low V_p/V_s ratios (1.7) for both average spinel and garnet + spinel peridotites (Figure 8 and Table 3). Anisotropy in V_p/V_s ratio due to the CPO might therefore partially explain the reduction in V_p/V_s ratio inferred by Chen et al. (2015) in the lithospheric mantle, with no need to invoke anomalous temperatures or partial melting, which are not corroborated by the study of the Tariat xenoliths.

Finally, SKS splitting in the Mongolian-Baikal deployment, which crosscuts the Hangay Dome in a N-S direction, is characterized by dominantly NW-SE fast S wave polarizations and highly variable, but in most cases, high delay times (1.5–2 s; Barruol et al., 2008). If as implied by the surface wave radial anisotropy, lineations in the lithospheric mantle are subhorizontal, vertically propagating SKS waves would sample very low birefringence ($\leq 2\%$) directions for both average spinel and garnet + spinel peridotites (Figure 8). This, together with the limited thickness of the lithospheric mantle inferred from the thermobarometry data on the xenoliths (≤ 50 km), implies a weak contribution of the lithospheric mantle (≤ 0.5 s) to the measured SKS delay times. The observed NW-SE fast direction corresponds indeed to the lower anisotropic layer detected for the ULN station, ~ 300 km east of the study area, which has been interpreted as recording the asthenospheric deformation in the region (Barruol et al., 2008). Yet such a weak contribution of the lithospheric mantle is not consistent with the strong variability in SKS splitting observed between neighboring stations across the array, suggesting that the Tariat xenolith CPOs reported here might not be representative of the entire lithospheric mantle beneath the region and that lateral variations in the lithospheric structure may occur at the scale of the dome.

5. Conclusions

All studied mantle peridotites from the Tariat region show clear olivine CPO indicative of deformation by dislocation creep under high T (> 1100 °C), moderate pressure (< 3 GPa), and dry conditions, consistent with the low hydrogen contents measured in olivine and both pyroxenes. They also show well-equilibrated microstructures, implying that ductile deformation was followed by static recrystallization, which annealed the deformation microstructure but preserved the CPO and, hence, the anisotropy of physical properties in the Hangay Dome mantle lithosphere.

The absence of nonannealed, high-stress, and high-strain microstructures suggests that the Tariat xenoliths have not sampled any domain in the lithospheric mantle submitted to recent deformation associated with the uplift of this region. The widespread annealing, independent of the equilibration temperatures of the xenoliths, and the lack of evidence for recent heating suggest that the static recrystallization is due to a long quiescence episode since the last deformation episode. Together, these observations corroborate previous interpretations based on surface deformation that the formation of the Hangay Dome is Mesozoic and not due to a recent (Cenozoic) mantle upwelling or plume.

The Tariat peridotites yield normal upper mantle seismic anisotropy patterns, characterized by fast polarization of S waves and fast propagation of P waves parallel to the mantle flow direction. The anisotropy intensity is variable among the studied xenoliths, but medium to low values predominate. The average spinel-peridotite and garnet + spinel peridotite samples show maximum P wave propagation anisotropy of 6.4% and 3.6% and maximum S wave polarization anisotropy of 4.5% and 2.9%. Moreover, the high proportion of fiber-[010] olivine CPO patterns results in dominantly low birefringence for S waves propagating at high angle to the flow plane. Thus, if as suggested from radial anisotropy measurements in the region, flow directions are subhorizontal, vertically propagating SKS waves should accumulate low delay times (≤ 0.5 s) in the lithospheric mantle and a large part of the observed signal should result from asthenospheric flow. The Tariat xenolith compositions, microstructures, equilibrium temperatures, and CPO may explain the weak P wave velocity anomalies, but not the strong low S wave velocity anomalies predicted by some tomographic models in the lithospheric mantle beneath the Hangay Dome. The petrostructural data for the xenoliths also are not consistent with the presence of substantial melting in the shallow mantle as interpreted based on the high conductivity inferred from MT data.

Acknowledgments

Many of the samples used in this study were collected with support from NSF grant EAR-1009494 to R. W. C. D. A. I. acknowledges funding for mantle studies from CNRS INSU-PNP grants. ANR INDIGO has also supported this study. The authors thank the Associate Editor and two anonymous reviewers whose comments have improved the initial manuscript. The data used in this article are given in the figures, tables, and supporting information, including the entire EBSD maps data set and corresponding CPO. Raw EBSD data are available upon request to the corresponding authors.

References

- Abramson, E. H., Brown, J. M., Slutsky, L. J., & Zaug, J. M. (1997). The elastic constants of San Carlos olivine to 17 GPa. *Journal of Geophysical Research*, 102, 12,253–12,263. <https://doi.org/10.1029/97JB00682>
- Afonso, J. C., Ranalli, G., Fernández, M., Griffin, W. L., O'Reilly, S. Y., & Faul, U. (2010). On the Vp/Vs–Mg# correlation in mantle peridotites: Implications for the identification of thermal and compositional anomalies in the upper mantle. *Earth and Planetary Science Letters*, 289(3–4), 606–618. <https://doi.org/10.1016/j.epsl.2009.12.005>
- Ancuta, L. D., Zeitler, P. K., Idleman, B. D., & Jordan, B. T. (2018). Whole-rock $^{40}\text{Ar}/^{39}\text{Ar}$ geochronology, geochemistry, and stratigraphy of intraplate Cenozoic volcanic rocks, central Mongolia. *Bulletin of the Geological Society of America*, 130(7–8), 1397–1408. <https://doi.org/10.1130/B31788.1>
- Bachmann, F., Hielscher, R., & Schaeben, H. (2010). Texture analysis with MTEX—Free and open source software toolbox. *Solid State Phenomena*, 160, 63–68. <https://doi.org/10.4028/www.scientific.net/SSP.160.63>
- Bali, E., Bolfan-Casanova, N., & Koga, K. (2008). Pressure and temperature dependence of H solubility in forsterite: An implication to water activity in the Earth interior. *Earth and Planetary Science Letters*, 268, 354–363.
- Barruol, G., Deschamps, A., Déverchère, J., Mordvinova, V. V., Ulziibat, M., Perrot, J., Artemiev, A. A., et al. (2008). Upper mantle flow beneath and around the Hangay Dome, central Mongolia. *Earth and Planetary Science Letters*, 274(1–2), 221–233. <https://doi.org/10.1016/j.epsl.2008.07.027>
- Barry, T. L., Ivanov, A. V., Rasskazov, S. V., Demonterova, E. I., Dunai, T. J., Davies, G. R., & Harrison, D. (2007). Helium isotopes provide no evidence for deep mantle involvement in widespread Cenozoic volcanism across central Asia. *Lithos*, 95(3–4), 415–424. <https://doi.org/10.1016/j.lithos.2006.09.003>
- Barry, T. L., & Kent, R. W. (1998). Cenozoic magmatism in Mongolia and the origin of central and East Asian basalts. In M. J. F. Flower, S.-L. Chung, C.-H. Lo, & T. Y. Lee (Eds.), *Mantle dynamics and plate interactions in East Asia*, *Geodynamics Series* 27 (pp. 347–366). Washington, DC: American Geophysical Union. <https://doi.org/10.1029/GD027p0347>
- Barry, T. L., Saunders, A. D., Kempton, P. D., Windley, B. F., Pringle, M. S., Dorjnamjaa, D., & Saandar, S. (2003). Petrogenesis of Cenozoic basalts from Mongolia: Evidence for the role of asthenospheric versus metasomatized lithospheric mantle sources. *Journal of Petrology*, 44(1), 55–91. <https://doi.org/10.1093/petrology/44.1.55>
- Bell, D. R., Ihinger, P. D., & Rossman, G. R. (1995). Quantitative and analysis of trace OH in garnet and pyroxenes. *American Mineralogist*, 80(5–6), 465–474. <https://doi.org/10.2138/am-1995-5-607>
- Bell, D. R., & Rossman, G. R. (1992). Water in Earth's mantle: The role of nominally anhydrous minerals. *Science*, 255(5050), 1391–1397. <https://doi.org/10.1126/science.255.5050.1391>
- Bell, D. R., Rossman, G. R., Maldener, J., Endisch, D., & Rauch, F. (2003). Hydroxide in olivine: A quantitative determination of the absolute amount and calibration of the IR spectrum. *Journal of Geophysical Research*, 108(B2), 2105. <https://doi.org/10.1029/2001JB000679>
- Brey, G. P., & Köhler, T. (1990). Geothermobarometry in four-phase lherzolite II. New thermobarometers, and practical assessment of existing thermobarometers. *Journal of Petrology*, 31(6), 1353–1378. <https://doi.org/10.1093/petrology/31.6.1353>
- Bunge, H.-J. (1982). *Texture analysis in materials science* (p. 593). London: Butterworths.
- Calais, E., Vergnolle, M., San'kov, V., Likhnev, A., Miroshnichenko, A., Amarjargal, S., & Déverchère, J. (2003). GPS measurements of crustal deformation in the Baikal-Mongolia area (1994–2002): Implications for current kinematics of Asia. *Journal of Geophysical Research*, 108(B10), 2501. <https://doi.org/10.1029/2002JB002373>
- Carlson, R. W., & Ionov, D. A. (2013). Preserving fertile MORB mantle in the continental lithosphere. *Mineralogical Magazine*, 77, 827.
- Chai, M., Brown, J. M., & Slutsky, L. J. (1997a). The elastic constants of an aluminous orthopyroxene to 12.5 GPa. *Journal of Geophysical Research*, 102, 14,779–14,785. <https://doi.org/10.1029/97JB00893>

- Chai, M., Brown, J. M., & Slutsky, L. J. (1997b). The elastic constants of a pyrope-grossular-almandine garnet to 20 GPa. *Geophysical Research Letters*, *24*, 523–526. <https://doi.org/10.1029/97GL00371>
- Chen, M., Niu, F., Liu, Q., & Tromp, J. (2015). Mantle-driven uplift of Hangai Dome: New seismic constraints from adjoint tomography. *Geophysical Research Letters*, *42*, 6967–6974. <https://doi.org/10.1002/2015GL065018>
- Comeau, M. J., Käufel, J. S., Becken, M., Kuvshinov, A., Grayver, A. V., Kamma, J., Demberel, S., et al. (2018). Evidence for fluid and melt generation in response to an asthenospheric upwelling beneath the Hangai Dome, Mongolia. *Earth and Planetary Science Letters*, *487*, 201–209. <https://doi.org/10.1016/j.epsl.2018.02.007>
- Cui, Z., Meltzer, A., Fischer, K. M., Stachnik, J.C., Munkhuu, U., Tsagaan, B., & Russ, R. M. (2017). Structure of lithospheric and upper mantle discontinuities beneath central Mongolia from receiver functions, American Geophysical Union Fall Meeting 2017, Abstract DI23A-0413.
- Cunningham, W. D. (1998). Lithospheric controls on late Cenozoic construction of the Mongolian Altai. *Tectonics*, *17*, 891–902. <https://doi.org/10.1029/1998TC900001>
- Cunningham, W. D. (2001). Cenozoic normal faulting and regional doming in the southern Hangay region, central Mongolia: Implications for the origin of the Baikal rift province. *Tectonophysics*, *331*(4), 389–411. [https://doi.org/10.1016/S0040-1951\(00\)00228-6](https://doi.org/10.1016/S0040-1951(00)00228-6)
- Demouchy, S., & Bolfan-Casanova, N. (2016). Distribution and transport of hydrogen in the lithospheric mantle: A review. *Lithos*, *240-243*, 402–425. <https://doi.org/10.1016/j.lithos.2015.11.012>
- Demouchy, S., Ishikawa, A., Tommasi, A., Alard, O., & Keshav, S. (2015). Characterization of hydration in the mantle lithosphere: Peridotite xenoliths from the Ontong Java Plateau as an example. *Lithos*, *212-215*, 189–201. <https://doi.org/10.1016/j.lithos.2014.11.005>
- Demouchy, S., Jacobsen, S. D., Gaillard, F., & Stern, C. R. (2006). Rapid magma ascent recorded by water diffusion profiles in mantle olivine. *Geology*, *34*(6), 429–432. <https://doi.org/10.1130/G22386.1>
- Denis, C. M. M., Alard, O., & Demouchy, S. (2015). Water content and hydrogen behaviour during metasomatism in the uppermost mantle beneath Ray Pic volcano (Massif Central, France). *Lithos*, *236-237*, 256–274. <https://doi.org/10.1016/j.lithos.2015.08.013>
- Denis, C. M. M., Demouchy, S., & Alard, O. (2018). Heterogeneous hydrogen distribution in orthopyroxene from veined mantle peridotite (San Carlos, Arizona): Impact of melt-rock interactions. *Lithos*, *302-303*, 298–311. <https://doi.org/10.1016/j.lithos.2018.01.007>
- Denis, C. M. M., Demouchy, S., & Shaw, C. (2013). Evidence of dehydration in peridotites from Eifel Volcanic Field and estimates of magma ascent rates. *Journal of Volcanology and Geothermal Research*, *258*, 85–99. <https://doi.org/10.1016/j.jvolgeores.2013.04.010>
- Dohmen, R., Chakraborty, S., & Becker, H. W. (2002). Si and O in olivine and implications for characterizing plastic flow in the mantle. *Journal of Geophysical Research*, *29*(21), 2030. <https://doi.org/10.1029/2002GL015480>
- Dohmen, R., & Milke, R. (2010). Diffusion in polycrystalline materials: Grain boundaries, mathematical models, and experimental data. In *Diffusion in minerals and melts* (pp. 921–970). Washington, DC: American Mineral Soc.
- Dziewonski, A. M., & Anderson, D. L. (1981). Preliminary reference Earth model. *Physics of the Earth and Planetary Interiors*, *25*(4), 297–356. [https://doi.org/10.1016/0031-9201\(81\)90046-7](https://doi.org/10.1016/0031-9201(81)90046-7)
- Faul, U., & Jackson, I. (2005). The seismological signature of temperature and grain size variations in the upper mantle. *Earth and Planetary Science Letters*, *234*(1-2), 119–134. <https://doi.org/10.1016/j.epsl.2005.02.008>
- Férot, A., & Bolfan-Casanova, N. (2012). Water storage capacity in olivine and pyroxene to 14 GPa: Implications for the water content of the Earth's upper mantle and nature of seismic discontinuities. *Earth and Planetary Science Letters*, *349-350*, 218–230. <https://doi.org/10.1016/j.epsl.2012.06.022>
- Foulger, G. R., Panza, G. F., Artemieva, I. M., Bastow, I. D., Cammarano, F., Evans, J. R., Hamilton, W. B., et al. (2013). Caveats on tomographic images. *Terra Nova*, *25*(4), 259–281. <https://doi.org/10.1111/ter.12041>
- Frets, E., Tommasi, A., Garrido, C. J., Vauchez, A., Mainprice, D., Targuisti, K., & Amri, I. (2014). The Beni Bousera peridotite (Morocco): An oblique-slip low-angle shear zone thinning the subcontinental mantle lithosphere. *Journal of Petrology*, *55*(2), 283–313. <https://doi.org/10.1093/petrology/egt067>
- Fuller, J., Lebedev, S., Agius, M. R., Jones, A. G., & Afonso, J. C. (2012). Lithospheric structure in the Baikal–central Mongolia region from integrated geophysical-petrological inversion of surface-wave data and topographic elevation. *Geochemistry, Geophysics, Geosystems*, *13*, Q0AK09. <https://doi.org/10.1029/2012GC004138>
- Gaetani, G. A., O'Leary, J. A., Koga, K. T., Hauri, E. H., Rose-Koga, E. F., & Monteleone, B. D. (2014). Hydration of mantle olivine under variable water and oxygen fugacity conditions. *Contributions to Mineralogy and Petrology*, *167*(2), 965. <https://doi.org/10.1007/s00410-014-0965-y>
- Gardés, E., Gaillard, F., & Tarits, P. (2014). Toward a unified hydrous olivine electrical conductivity law. *Geochemistry, Geophysics, Geosystems*, *15*, 4984–5000. <https://doi.org/10.1002/2014GC005496>
- Green, D. H., Hibberson, W. O., Rosenthal, A., Kovács, I., Yaxley, G. M., Falloon, T. J., & Brink, F. (2014). Experimental study of the influence of water on melting and phase assemblages in the upper mantle. *Journal of Petrology*, *55*(10), 2067–2096. <https://doi.org/10.1093/petrology/egu050>
- Hielscher, R., & Schaeben, H. (2008). A novel pole figure inversion method: Specification of the MTEX algorithm. *Journal of Applied Crystallography*, *41*(6), 1024–1037. <https://doi.org/10.1107/S0021889808030112>
- Higgie, K., & Tommasi, A. (2012). Feedbacks between deformation and melt distribution in the crust-mantle transition zone of the Oman ophiolite. *Earth and Planetary Science Letters*, *359-360*, 61–72. <https://doi.org/10.1016/j.epsl.2012.10.003>
- Higgie, K., & Tommasi, A. (2014). Deformation of a partially molten mantle: Constraints from plagioclase-lherzolites from Lanzo, western Alps. *Tectonophysics*, *615-616*, 167–181. <https://doi.org/10.1016/j.tecto.2014.01.007>
- Hiraga, T., Tachibana, C., Ohashi, N., & Sano, S. (2010). Grain growth systematics for forsterite ± enstatite aggregates: Effect of lithology on grain size in the upper mantle. *Earth and Planetary Science Letters*, *291*(1-4), 10–20. <https://doi.org/10.1016/j.epsl.2009.12.026>
- Ingrin, J., & Skogby, H. (2000). Hydrogen in nominally anhydrous upper-mantle minerals: Concentration levels and implications. *European Journal of Mineralogy*, *12*(3), 543–570. <https://doi.org/10.1127/ejm/12/3/0543>
- Ionov, D. (2002). Mantle structure and rifting processes in the Baikal-Mongolia region: Geophysical data and evidence from xenoliths in volcanic rocks. *Tectonophysics*, *351*(1-2), 41–60. [https://doi.org/10.1016/S0040-1951\(02\)00124-5](https://doi.org/10.1016/S0040-1951(02)00124-5)
- Ionov, D. A. (1986). Spinel peridotite xenoliths from the Shavaryn-Tsaram volcano, northern Mongolia: Petrography, major element chemistry and mineralogy. *Geologica Carpathica*, *37*, 681–692.
- Ionov, D. A. (2007). Compositional variations and heterogeneity in fertile lithospheric mantle: Peridotite xenoliths in basalts from Tariat, Mongolia. *Contributions to Mineralogy and Petrology*, *154*(4), 455–477. <https://doi.org/10.1007/s00410-007-0203-y>
- Ionov, D. A., Bushlyakov, I. N., & Kovalenko, V. I. (1986). The content of F and Cl in phlogopites, amphibole, and apatite in mantle xenoliths from Shavaryn-Tsaram maar in Mongolia. *Transactions of the USSR Academy of Science: Earth Science Section*, *287*, 174–177.

- Ionov, D. A., Griffin, W. L., & O'Reilly, S. Y. (1997). Volatile-bearing minerals and lithophile trace elements in the upper mantle. *Chemical Geology*, 141(3-4), 153–184. [https://doi.org/10.1016/S0009-2541\(97\)00061-2](https://doi.org/10.1016/S0009-2541(97)00061-2)
- Ionov, D. A., & Hofmann, A. W. (2007). Depth of formation of subcontinental off-craton peridotites. *Earth and Planetary Science Letters*, 261(3-4), 620–634. <https://doi.org/10.1016/j.epsl.2007.07.036>
- Ionov, D. A., Hofmann, A. W., & Shimizu, N. (1994). Metasomatism-induced melting in mantle xenoliths from Mongolia. *Journal of Petrology*, 35(3), 753–785. <https://doi.org/10.1093/ptrology/35.3.753>
- Ionov, D. A., O'Reilly, S. Y., & Griffin, W. L. (1998a). Off-Cratonic garnet and spinel peridotite xenoliths from Dsun-Bussular, SE Mongolia. 7th International Kimberlite Conference, Cape Town, 383–389.
- Ionov, D. A., O'Reilly, S. Y., & Griffin, W. L. (1998b). A geotherm and lithospheric cross-section for central Mongolia. In M. J. F. Flower, S.-L. Chung, C.-H. Lo, & T. Y. Lee (Eds.), *Mantle dynamics and plate interactions in East Asia, Geodynamics Series* (Vol. 27, pp. 127–153). Washington, DC: American Geophysical Union. <https://doi.org/10.1029/GD027p0127>
- Jackson, I., & Faul, U. H. (2010). Grainsize-sensitive viscoelastic relaxation in olivine: Towards a robust laboratory-based model for seismological application. *Physics of the Earth and Planetary Interiors*, 183(1-2), 151–163. <https://doi.org/10.1016/j.pepi.2010.09.005>
- Jacobsen, S. D. (2006). Effect of water on the equation of state of nominally anhydrous minerals. *Reviews in Mineralogy and Geochemistry*, 62(1), 321–342. <https://doi.org/10.2138/rmg.2006.62.14>
- Katz, R. F., Spiegelman, M., & Langmuir, C. H. (2003). A new parameterization of hydrous mantle melting. *Geochemistry, Geophysics, Geosystems*, 4(9), 1073. <https://doi.org/10.1029/2002GC000433>
- Kennett, B. L. N., Engdahl, E. R., & Buland, B. (1995). Constraints on seismic velocities in the Earth from traveltimes. *Geophysical Journal International*, 122(1), 108–124. <https://doi.org/10.1111/j.1365-246X.1995.tb03540.x>
- Khutorskoy, M., & Yarmoluk, V. (1989). Heat flow, structure and evolution of the lithosphere of Mongolia. *Tectonophysics*, 164(2-4), 315–322. [https://doi.org/10.1016/0040-1951\(89\)90024-3](https://doi.org/10.1016/0040-1951(89)90024-3)
- Koizumi, S., Hiraga, T., Tasaka, M., Tachibana, C., Miyazaki, T., Kobayashi, T., & Takamasa, A. (2010). Synthesis of highly dense and fine-grained aggregates of mantle composites by vacuum sintering of nano-sized mineral powders. *Physics and Chemistry of Minerals*, 37(8), 505–518. <https://doi.org/10.1007/s00269-009-0350-y>
- Koulakov, I. (2011). High-frequency *P* and *S* velocity anomalies in the upper mantle beneath Asia from inversion of worldwide traveltime data. *Journal of Geophysical Research*, 116, B04301. <https://doi.org/10.1029/2010JB007938>
- Kovács, I., Green, H. W., Rosenthal, A., Hermann, J., O'Neill, H. S. C., Hiberson, W. O., & Udvardi, B. (2012). An experimental study of water in nominally anhydrous minerals in the upper mantle near water-saturated solidus. *Journal of Petrology*, 53(10), 2067–2093. <https://doi.org/10.1093/ptrology/egs044>
- Lebedev, S., Meier, T., & van der Hilst, R. D. (2006). Asthenospheric flow and origin of volcanism in the Baikal rift area. *Earth and Planetary Science Letters*, 249(3-4), 415–424. <https://doi.org/10.1016/j.epsl.2006.07.007>
- Lebedev, S., & van der Hilst, R. D. (2008). Global upper-mantle tomography with the automated multimode inversion of surface and *S*-wave forms. *Geophysical Journal International*, 173(2), 505–518. <https://doi.org/10.1111/j.1365-246X.2008.03721.x>
- Lee, C.-T. A. (2003). Compositional variation of density and seismic velocities in natural peridotites at STP conditions: Implications for seismic imaging of compositional heterogeneities in the upper mantle. *Journal of Geophysical Research*, 108(B9), 2441. <https://doi.org/10.1029/2003JB002413>
- Lysak, S., & Dorofeeva, R. (2003). Thermal state of the lithosphere in Mongolia. *Russian Geology and Geophysics*, 44(9), 893–903.
- Mainprice, D. (1990). A fortran program to calculate seismic anisotropy from the lattice preferred orientation of minerals. *Computers and Geosciences*, 16(3), 385–393. [https://doi.org/10.1016/0098-3004\(90\)90072-2](https://doi.org/10.1016/0098-3004(90)90072-2)
- Mainprice, D., Bachmann, F., Hielscher, R., & Schaeben, H. (2014). Descriptive tools for the analysis of texture projects with large datasets using MTEX: Strength, symmetry and components. In D. R. Faulkner, E. Mariani, & J. Mecklenburgh (Eds.), *Rock deformation from field, experiments and theory: A volume in honour of Ernie Rutter, Geological Society, London, Special Publications* (Vol. 409, pp. 251–271). <https://doi.org/10.1144/SP409.8>
- McDannell, K. T., Zeitler, P. K., & Idleman, B. D. (2018). Relict topography within the Hangay Mountains in central Mongolia: Quantifying long-term exhumation and relief change in an old landscape. *Tectonics*, 37, 1–28. <https://doi.org/10.1029/2017TC004682>
- McDonough, W. F., & Sun, S.-S. (1995). The composition of the Earth. *Chemical Geology*, 120, 223–253.
- Mierdel, K., Keppler, H., Smyth, J. R., & Langerhorst, F. (2007). Water solubility in aluminous orthopyroxene and the origin of the asthenosphere. *Science*, 315(5810), 364–368. <https://doi.org/10.1126/science.1135422>
- Miller, G. H., Rossman, G. R., & Harlow, G. E. (1987). The natural occurrence of hydroxide in olivine. *Physics and Chemistry of Minerals*, 14(5), 461–472. <https://doi.org/10.1007/BF00628824>
- Nickel, K. G., & Green, D. H. (1985). Empirical geothermobarometry for garnet peridotites and implication for the nature of lithosphere, kimberlites and diamonds. *Earth and Planetary Science Letters*, 73(1), 158–170. [https://doi.org/10.1016/0012-821X\(85\)90043-3](https://doi.org/10.1016/0012-821X(85)90043-3)
- O'Neill, H. S. C. (1981). The transition between spinel lherzolite and garnet lherzolite, and its use as a geobarometer. *Contribution to Mineralogy and Petrology*, 77, 185–194.
- Palme, H., & O'Neill, H. S. C. (2003). Cosmochemical estimates of mantle composition. In R. W. Carlson (Ed.), *Treatise on geochemistry, The mantle and core* (Vol. 2, pp. 1–38). Amsterdam: Elsevier.
- Paterson, M. S. (1982). The determination of hydroxyl by infrared absorption in quartz, silicate glasses and similar materials. *Bulletin de Mineralogie*, 105, 20–29.
- Peslier, A., Luhr, J., & Post, J. (2002). Low water contents in pyroxenes from spinel-peridotites of the oxidized, sub-arc mantle wedge. *Earth and Planetary Science Letters*, 201(1), 69–86. [https://doi.org/10.1016/S0012-821X\(02\)00663-5](https://doi.org/10.1016/S0012-821X(02)00663-5)
- Peslier, A., & Luhr, J. F. (2006). Hydrogen loss from olivines in mantle xenoliths from Simcoe (USA) and Mexico: Mafic alkalic magma ascent rate and water budget of the sub-continental lithosphere. *Earth and Planetary Science Letters*, 242(3-4), 302–319. <https://doi.org/10.1016/j.epsl.2005.12.019>
- Peslier, A. H. (2010). A review of water contents of nominally anhydrous minerals in the mantles of Earth, Mars and the Moon. *Journal of Volcanology and Geothermal Research*, 197(1-4), 239–258. <https://doi.org/10.1016/j.jvolgeores.2009.10.006>
- Petit, C., Burov, E., & Tiberi, C. (2008). Strength of the lithosphere and strain localisation in the Baikal rift. *Earth and Planetary Science Letters*, 269(3-4), 523–529. <https://doi.org/10.1016/J.epsl.2008.03.012>
- Petit, C., Deverchère, J., Calais, E., San'kov, V., & Fairhead, D. (2002). Deep structure and mechanical behavior of the lithosphere in the Hangai-Hövsgöl region, Mongolia: New constraints from gravity modeling. *Earth and Planetary Science Letters*, 197(3-4), 133–149. [https://doi.org/10.1016/S0012-821X\(02\)00470-3](https://doi.org/10.1016/S0012-821X(02)00470-3)
- Press, S., Witt, G., Seck, H. A., Eonov, D., & Kovalenko, V. I. (1986). Spinel peridotite xenoliths from the Tariat Depression, Mongolia. I: Major element chemistry and mineralogy of a primitive mantle xenolith suite. *Geochimica et Cosmochimica Acta*, 50, 2587–2599.

- Qi, C., Hansen, L. N., Wallis, D., Holtzman, B. K., & Kohlstedt, D. L. (2018). Crystallographic preferred orientation of olivine in sheared partially molten rocks: The source of the “a-c switch”. *Geochemistry, Geophysics, Geosystems*, 19, 316–336. <https://doi.org/10.1002/2017GC007309>
- Sang, L., & Bass, J. D. (2014). Single-crystal elasticity of diopside to 14 GPa by Brillouin scattering. *Physics of the Earth and Planetary Interiors*, 228, 75–79. <https://doi.org/10.1016/j.pepi.2013.12.011>
- Satsukawa, T., Godard, M., Demouchy, S., Michibayashi, K., & Ildefonse, B. (2017). Chemical interactions in the subduction factory: New insights from an in situ trace element and hydrogen study of the Ichinomegata and Oki-Dogo mantle xenoliths (Japan). *Geochimica et Cosmochimica Acta*, 208, 234–267. <https://doi.org/10.1016/j.gca.2017.03.042>
- Skogby, H. (2006). Water in natural mantle minerals I: Pyroxenes. In *Water in nominally anhydrous minerals* (pp. 155–167). Chantilly, VA: American Mineralogical Society Geochemical Society.
- Soustelle, V., Tommasi, A., Demouchy, S., & Franz, L. (2013). Melt-rock interactions, deformation, hydration and seismic properties in the sub-arc lithospheric mantle inferred from xenoliths from seamounts near Lihir, Papua New Guinea. *Tectonophysics*, 608, 330–345. <https://doi.org/10.1016/j.tecto.2013.09.024>
- Souza, S. (2015). Upper mantle structure beneath the Hangay Dome, central Mongolia and implications for high topography and magmatism. Theses and dissertations. 2821. [h5p://preserve.lehigh.edu/Etd/2821](https://preserve.lehigh.edu/Etd/2821)
- Stosch, H. G., Ionov, D. A., Puchtel, I. S., Galer, S. J. G., & Sharpouri, A. (1995). Lower crustal xenoliths from Mongolia and their bearing on the nature of the deep crust beneath central Asia. *Lithos*, 36(3–4), 227–242. [https://doi.org/10.1016/0024-4937\(95\)00019-4](https://doi.org/10.1016/0024-4937(95)00019-4)
- Streckeisen, A. (1976). To each plutonic rock its proper name. *Earth-Science Reviews*, 12(1), 1–33. [https://doi.org/10.1016/0012-8252\(76\)90052-0](https://doi.org/10.1016/0012-8252(76)90052-0)
- Tiberi, C., Deschamps, A., Déverchère, J., Petit, C., Perrot, J., Appriou, D., Mordvinova, V., et al. (2008). Asthenospheric imprints on the lithosphere in central Mongolia and southern Siberia from a joint inversion of gravity and seismology (MOBAL experiment). *Geophysical Journal International*, 175(3), 1283–1297. <https://doi.org/10.1111/j.1365-246X.2008.03947.x>
- Tommasi, A., Godard, M., Coromina, G., Dautria, J. M., & Barszczus, H. (2004). Seismic anisotropy and compositionally-induced velocity anomalies in the lithosphere above mantle plumes: A petrological and microstructural study of mantle xenoliths from French Polynesia. *Earth and Planetary Science Letters*, 227, 539–556.
- Tommasi, A., Mainprice, D., Canova, G., & Chastel, Y. (2000). Viscoplastic self-consistent and equilibrium-based modeling of olivine lattice preferred orientations. Implications for the upper mantle seismic anisotropy. *Journal of Geophysical Research*, 105, 7893–7908. <https://doi.org/10.1029/1999JB900411>
- Tommasi, A., Tikoff, B., & Vauchez, A. (1999). Upper mantle tectonics: Three-dimensional deformation, olivine crystallographic fabrics and seismic properties. *Earth and Planetary Science Letters*, 168(1–2), 173–186. [https://doi.org/10.1016/S0012-821X\(99\)00046-1](https://doi.org/10.1016/S0012-821X(99)00046-1)
- Tommasi, A., Vauchez, A., & Ionov, D. A. (2008). Deformation, static recrystallization, and reactive melt transport in shallow subcontinental mantle xenoliths (Tok Cenozoic volcanic field, SE Siberia). *Earth and Planetary Science Letters*, 272(1–2), 65–77. <https://doi.org/10.1016/j.epsl.2008.04.020>
- Vauchez, A., Tommasi, A., & Mainprice, D. (2012). Faults (shear zones) in the Earth’s mantle. *Tectonophysics*, 558–559, 1–27. <https://doi.org/10.1016/j.tecto.2012.06.006>
- Vergnolle, M., Calais, E., & Dong, L. (2007). Dynamics of continental deformation in Asia. *Journal of Geophysical Research*, 112, B11403. <https://doi.org/10.1029/2006JB004807>
- Wang, Q. (2010). A review of water contents and ductile deformation mechanisms of olivine: Implications for the lithosphere–asthenosphere boundary of continents. *Lithos*, 120(1–2), 30–41. <https://doi.org/10.1016/j.lithos.2010.05.010>
- Windley, B. F., & Allen, M. B. (1993). Mongolian plateau: Evidence for a late Cenozoic mantle plume under central Asia. *Geology*, 21(4), 295–299. [https://doi.org/10.1130/0091-7613\(1993\)021<0295:MPEFAL>2.3.CO;2](https://doi.org/10.1130/0091-7613(1993)021<0295:MPEFAL>2.3.CO;2)
- Withers, A. C., Bureau, H., Raepsaet, C., & Hirschmann, M. M. (2012). Calibration of infrared spectroscopy by elastic recoil detection analysis of H in synthetic olivine. *Chemical Geology*, 334, 92–98. <https://doi.org/10.1016/j.chemgeo.2012.10.002>
- Xia, Q. K., Hao, Y., Deloule, E., Coltorti, M., Dallai, L., Yang, X., & Feng, M. (2010). Low water content of the Cenozoic lithosphere mantle beneath the eastern part of North China Craton. *Journal of Geophysical Research*, 115, B07207. <https://doi.org/10.1029/2009JB006694>
- Yoshino, T., Matsuzaki, T., Yamashita, S., & Katsura, T. (2006). Hydrous olivine unable to account for conductivity anomaly at the top of the asthenosphere. *Nature*, 443(7114), 973–976. <https://doi.org/10.1038/nature05223>
- Yu, Y., Xu, X.-S., Griffin, W. L., O’Reilly, S. Y., & Xia, Q.-K. (2011). H₂O contents and their modification in the Cenozoic subcontinental lithospheric mantle beneath the Cathaysia block, SE China. *Lithos*, 126, 1–16.
- Zorin, Y. A. (1999). Geodynamics of the western part of the Mongolia–Okhotsk collisional belt, Trans-Baikal region (Russia) and Mongolia, 1999. Geodynamics of the western part of the Mongolia–Okhotsk collisional belt, Trans-Baikal region (Russia) and Mongolia. *Tectonophysics*, 306(1), 33–56. [https://doi.org/10.1016/S0040-1951\(99\)00042-6](https://doi.org/10.1016/S0040-1951(99)00042-6)